buildings

MDPI

Article

Effect of Geometric Parameters on the Behavior of Eccentric RC Beam–Column Joints

Mostafa A. Abdel-Latif [1], Amr A. Nassr [1,2,*], Wojciech Sumelka [3], Mohamed M. Mohamed [1], Aly G. Abd El-Shafi [1] and Eslam Soliman [1]

[1] Department of Civil Engineering, Assiut University, Assiut 71516, Egypt; mostafa_ahmed@eng.au.edu.eg (M.A.A.-L.); mohamed.mohamed33@eng.au.edu.eg (M.M.M.); agaly@aun.edu.eg (A.G.A.E.-S.); esoliman@aun.edu.eg (E.S.)
[2] Department of Civil Engineering, Ajman University, Ajman P.O. Box 346, United Arab Emirates
[3] Institute of Structural Analysis, Poznan University of Technology, Piotrowo 5, 60-965 Poznan, Poland; wojciech.sumelka@put.poznan.pl
* Correspondence: a.nassr@ajman.ac.ae

Abstract: Over the last century, the seismic behavior of reinforced concrete (RC) beam–column joints has drawn many researchers' attention due to their complex stress state. Such joints should possess sufficient capacity and ductility to ensure integrity and safety when subjected to cyclic loading during seismic events. In the literature, while most studies have focused on the behavior of concentric beam–column joints, few studies investigated the response of eccentric beam–column joints, in which the beam's centerline is offset from the centerline of the column. Recent earthquakes demonstrated severe damage in eccentric beam–column joints due to their brittle torsional behavior, which may threaten the ductility required for the overall structural performance. To investigate the effect of brittle failure on the strength, ductility, and stability of eccentric beam–column joints, nonlinear finite element (FE) models were developed and validated. The FE model was employed to study the effect of some geometric parameters on the global and local behaviors of beam–column joints, including the joint type (exterior and interior), the column aspect ratio, and the joint aspect ratio. The results show that the joint aspect ratio, which is the ratio of beam-to-column depth, has a predominant effect on the failure behavior of the joint. Additionally, the increase in column aspect ratio alters the failure mode from brittle joint shear failure to ductile beam-hinge, although there is an increase in the joint torsional moment. The current study also showed that interior joints exhibited a higher out-of-plane moment as well as more extensive column torsion cracks compared to exterior joints.

Keywords: beam–column; joint; eccentricity; reinforced concrete; nonlinear finite element; modeling; torsion

check for updates

Citation: Abdel-Latif, M.A.; Nassr, A.A.; Sumelka, W.; Mohamed, M.M.; Abd El-Shafi, A.G.; Soliman, E. Effect of Geometric Parameters on the Behavior of Eccentric RC Beam–Column Joints. *Buildings* **2023**, *13*, 1980. https://doi.org/10.3390/buildings13081980

Academic Editors: Rajai Zuheir Al-Rousan and Binsheng (Ben) Zhang

Received: 21 June 2023
Revised: 20 July 2023
Accepted: 20 July 2023
Published: 2 August 2023

Copyright: © 2023 by the authors. Licensee MDPI, Basel, Switzerland. This article is an open access article distributed under the terms and conditions of the Creative Commons Attribution (CC BY) license (https://creativecommons.org/licenses/by/4.0/).

1. Introduction

Beam–column joints are the most critical zones in reinforced concrete (RC) moment-resisting frames to withstand seismic loads due to the complex stress state and insufficient ductility compared to other structural components. The inelastic behavior of beam–column joints has been studied since the 1960s [1–3]. These studies have served as a basis for the design of beam–column joints, in which details of the requirements and stress limits are given to control the damage and deterioration of strength and stiffness in the connections [4–6]. Previous research on RC connections has mainly focused on the concentric configuration between the column and beam [4,7]. On the other hand, limited studies have examined the behavior of eccentric joints where the beam's centerline is offset, in the plan, from the column centerline. Such eccentric joints are widely constructed, mainly in the perimeters of RC buildings.

The effect of joint eccentricity and other geometrical properties on the behavior of RC beam–column joints subjected to reverse-cyclic lateral loading has been examined [8–13].

In the early 1990s, Joh et al. [8], Lawrance et al. [9], and Raffaelle and Wight [13] observed early loss of strength and low ductility of cruciform eccentric beam–column joints due to the noticeable development of torsional cracks. Kusuhara et al. [11] demonstrated the effect of out-of-plane and torsion moments leading to a nonsymmetric yielding in beam reinforcement. Matsumoto et al. [14] emphasized that the reduction in shear strength of eccentric joints could be minimized with an eccentricity ratio, which is the ratio of the beam shift distance to the column width, below 0.25. Raffaele and Wight [13] highlighted the significance of the column aspect ratio on the failure behavior of eccentric beam–column joints. Teng and Zhou [15] tested six interior eccentric beam–column joints with various column aspect ratios and eccentricity ratios. They reported that the increase in eccentricity slightly impacted the joint subassemblies' global behavior while massively affecting the joint shear distortion. Lee and Ko [16] showed a significant degradation in the joint capacity associated with an increase in the eccentricity ratio from 0.125 to 0.25. Moreover, Burak and Wight [17] indicated that the entire column cross-section works to resist the joint force when its aspect ratio is less than or equal to 1.5. The seismic performance of eccentric knee connections has also been assessed by Mogili et al. [18], with a column aspect ratio of 1.4 and a normalized eccentricity of 0.14. The authors observed lower shear capacity and energy dissipation in the joint opening action compared to concentric joints. Chen and Chen [19] have proposed a geometrical configuration for minimizing the torsional moment and maximizing the effective joint area via expanding the beam width at the beam and column interface, resulting in a remarkable improvement in the global and local behaviors of the joint subassembly.

In addition to the geometrical properties, other factors that influence the failure behavior of eccentric beam–column joints, such as joint reinforcement and level of axial load, were also investigated. Ma et al. [20] and Wong et al. [21] reported that increasing the joint reinforcement helped to improve the plastic deformation capacity and delay the joint deterioration. Goto and Joh [22] and Kusuhara et al. [11] have noted the same results with increased shear reinforcement at the joint region. It was also found that slab reinforcement helps to move the acting line of the resultant force away from the flush face, thus reducing the torsional demand caused by eccentricity [10,14,17,20]. Furthermore, Lee and Yu [23] observed considerable improvements in the seismic behavior of the eccentric beam–column joints using single- and double-headed bars. Moreover, the high level of the column axial load tends to minimize the wide column's maximum torsional angle and to provide a minor enhancement in the energy dissipation and stiffness before bond failure [24,25].

It is noted from the literature that there is a scarcity of investigations on eccentric joints, especially with various geometrical configurations. This highlights the need for further studies to understand eccentric joint behavior better [26]. Currently, the design provisions of ACI-318 [27] and ACI-352 [26] are found to underestimate eccentric beam–column joint shear capacity [12]. This paper investigated the effect of various geometric design parameters on the failure behavior of eccentric joints. To do so, a finite element model (FEM) was developed and calibrated using the data available in the literature. The calibration models were further extended to study the effects of joint type (exterior or interior), column aspect ratio, and joint aspect ratio (beam-to-column depth ratio) on the global and local behaviors of the eccentric RC beam–column joint subassemblies.

The present study deals with the smeared crack modeling approach, in which local discontinuities (i.e., cracks) are distributed over a specific area within finite elements [28]. One of the most popular smeared crack concrete models is the concrete damage plasticity model (CDP), proposed by Lubliner et al. [29], developed by Lee and Fenves [30], and implemented in ABAQUS [31]. Because of the high computational cost of nonlinear analysis of RC structures, especially for fine mesh sizes between 25 mm and 12.5 mm [32–34], many researchers [35–40] successfully obtain the detailed behaviors of different structural elements tested under cyclic loading (i.e., load–displacement backbone curves, cracking patterns,

yielding in reinforcement bars) by adopting monotonic loads through the CDP model. On the other side, several researchers [41–46] failed to obtain the cyclic characteristics of different structural responses for elements modeled via CDP even at a 30 mm mesh element size [47]. As a result, monotonic loading is typically preferred over cyclic loading when using the CDP model due to the absence of shear retention, which can lead to improper capture of the pinching behavior during load cycles in shear-dominated scenarios [48]. While continuum FEM can be impractical for design or extensive parametric studies compared to physics-based models [49], it offers detailed insights into the internal distribution of stress and strain, as well as the initiation and development of cracking patterns [50]. As such, it is often used in conjunction with laboratory tests and can serve as an alternative means of filling gaps in the data used to develop physics-based models.

2. Reference Tests for Calibration

The experimental results of two full-scale eccentric beam–column joints (exterior and interior) were utilized to calibrate and validate the FE model. The geometry and reinforcement details for both joint subassemblies are shown in Figure 1a,b. The first joint in Figure 1a, denoted as W150, is an exterior joint examined by Lee and Ko [16] and was designed according to the ACI-318 and ACI-352 guidelines. The specimen was constructed using concrete with a 28-day compressive strength of 29.5 MPa and a grade ASTM A706 [51] steel reinforcement for the longitudinal bars and stirrups. The second specimen in Figure 1b, denoted as J−10, is an interior joint tested by Matsumoto et al. [14] and was designed according to the Japanese code guidelines AJI [52]. The interior joint was constructed using concrete with a 28-day compressive strength and Young's modulus of elasticity of 57 MPa and 36 GPa, respectively. In addition, steel grades USD685 [53] and SBPD1275/1420 [54] were used for the longitudinal rebars and stirrups, respectively.

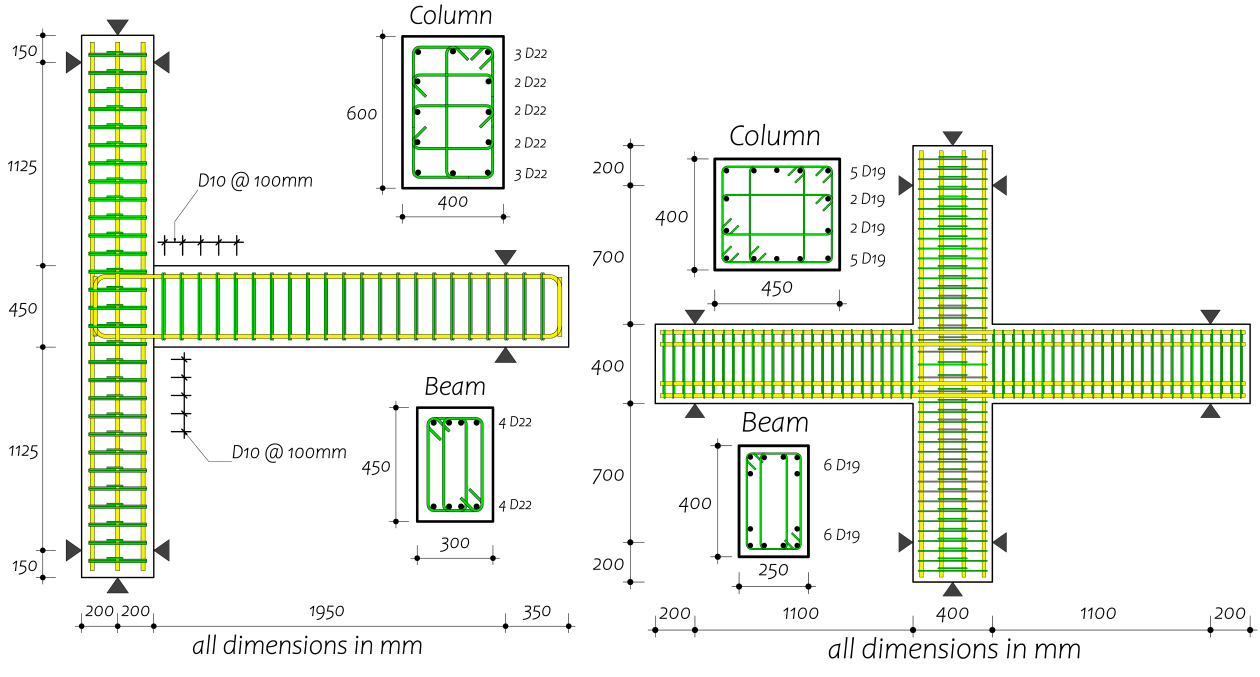

Figure 1. Reinforcement and geometric details of the experimental eccentric joint subassemblies used to validate the FE model: (**a**) exterior joint (W150) (adapted from Lee and Ko [16]), and (**b**) interior joint (J−10) (adapted from Matsumoto et al. [14]).

The exterior and interior joints had column aspect ratios of 1.5 and 1.125, while the eccentricity ratios were 0.25 and 0.22, respectively. Furthermore, the joint aspect ratios

were 1.125 and 1.0, respectively. The exterior joint exhibited joint deterioration after the beam plastic hinge development, known as beam-joint (BJ) failure mode [4]. In contrast, the interior joint showed early joint distortion even before the beam yield, which refers to the joint (J) failure mechanism [4]. Before applying cyclic load to the beams, axial forces equivalent to $0.1A_g f_{cm}$ and $0.2A_g f_{cm}$, where A_g is the gross area of the column and f_{cm} is the mean concrete compressive strength, were applied to the columns of the exterior and interior joint subassemblies, respectively. Both researchers reported that the columns' ends were fully restrained against column rotation around the vertical axis. Moreover, the cyclic load schedules, as shown in Figure 2, were applied to the beam, not the column. As a result, the P-Δ effect was minimized.

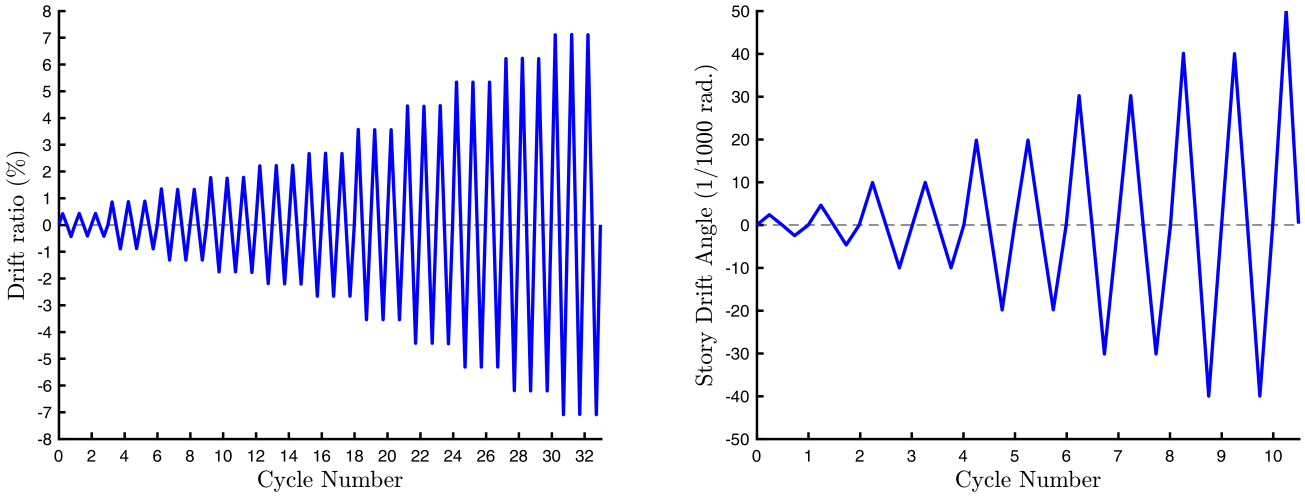

(**a**) (**b**)

Figure 2. Cyclic load schedules used in the experiments: (**a**) exterior joint (W150), and (**b**) interior joint (J−10).

3. Finite Element Model Details

Nonlinear finite element analysis performance and quality depend on all its fundamental components: the material constitutive model, finite element discretization, and solution approach. In this paper, the numerical model was developed using the ABAQUS® finite element software package [31]. The details of the material constitutive model, model geometry and meshing, boundary conditions, and simulation parameters are discussed below.

3.1. Material Constitutive Models

3.1.1. Concrete

The concrete material was modeled using linear elastic isotropic and CDP models for uncracked and cracked material, respectively. For the elastic properties, the initial modulus of elasticity E_{ci} for concrete was determined following the CEB-FIP model [55] as follows:

$$E_{ci} = E_{c0}\,\alpha_E \left(\frac{f_{cm}}{10}\right)^{1/3} \tag{1}$$

where E_{c0} is 21.5×10^3 MPa, and α_E is assumed here as 0.9 for limestone aggregates. An average value of 0.2 for Poisson's ratio ν is considered, which is a reasonable assumption for concrete material with a compressive strength ranging between 20 MPa and 120 MPa [56].

CDP was selected due to its unique plasticity mechanics, which describes the concrete pressure sensitivity and the irreversible deformation [57], while the damage can represent material deterioration due to cracking or crushing [58]. For concrete cracking, CDP utilizes the smeared crack model with a fixed orthogonal crack direction [59], where the crack

initiation is detected by the simple Rankine criterion [60]. Furthermore, the yield function of CDP was modified based on the classical Drucker–Prager yield function [29,30]. For both nonlinear compression and tension models, the crack band model was utilized to minimize the pathological sensitivity of the numerical results to discretization parameters such as the element size in finite element simulations. The crack band model guarantees that the same amount of energy (i.e., the tensile fracture energy G_{ft} and the compressive crushing energy G_{fc}) is dissipated during failures, independent of the element size [61].

For the compression behavior of concrete, the stress–strain curve consists of three stages, as shown in Figure 3a. The first stage is linear elastic up to a stress of $0.4f_{cm}$, in which the stresses and strains are governed by the secant modulus of elasticity E_c at concrete stress of $0.4f_{cm}$ following Equations (2) and (3). The second stage is the strain-hardening part for concrete stress ranging between $0.4f_{cm}$ and f_{cm}. The stress in concrete in this stage $\sigma_{c(2)}$ is computed following the expression proposed by the FIB model code (2010) in Equations (4) and (5). In these equations, ε_c and ε_{cm} represent the compressive strain and the strain at the compressive strength, respectively.

$$E_{c(1)} = E_c\,\varepsilon_c \tag{2}$$

$$E_c = \left(0.8 + 0.2\frac{f_{cm}}{88}\right)E_{ci} \tag{3}$$

$$\sigma_{c(2)} = \frac{E_{ci}\frac{\varepsilon_c}{f_{cm}} - \left(\frac{\varepsilon_c}{\varepsilon_{cm}}\right)^2}{1 + \left(E_{ci}\frac{\varepsilon_{cm}}{f_{cm}} - 2\right)\frac{\varepsilon_c}{\varepsilon_{cm}}}f_{cm} \tag{4}$$

$$\varepsilon_{cm} = 1.6\left(\frac{f_{cm}}{10}\right)^{0.25} \times 10^{-3} \tag{5}$$

The third stage represents the strain-softening part for concrete passing the peak stress f_{cm} till complete crushing failure. The concrete stress in this stage depends on the compressive crushing energy G_{fc} and the mesh size l_{ch}, following the formulas of Krätzig and Pölling [62] in Equations (6) and (7). To determine the crushing energy, Equation (8) was adopted, where the ratio of the crushing energy to the fracture energy can be assumed to be proportional to the square of the ratio of the compressive strength to the tensile strength [63,64]. It was noted through the calibration process that the induced energy from Equation (8) overestimates the post-peak responses of both connections. For this reason, half of the induced crushing energy obtained from Equation (8) was adapted in the FEM. In Equations (6)–(8) ε_c^{pl}, ε_c^{in}, and f_{tm} are the compressive damaged plastic strain, the compressive inelastic strain, and the main tensile strength, respectively.

$$\sigma_{c(3)} = \frac{1}{\left(\frac{2+\gamma_c f_{cm}\varepsilon_{cm}}{2f_{cm}} - \gamma_c\varepsilon_c + \frac{\varepsilon_c^2\gamma_c}{2\varepsilon_{cm}}\right)} \tag{6}$$

$$\gamma_c = \frac{\pi^2 f_{cm}\varepsilon_{cm}}{2\left[\frac{G_{fc}}{l_{ch}} - 0.5f_{cm}\left(\varepsilon_{cm}(1-b) + b\frac{f_{cm}}{E_c}\right)\right]^2},\ b = \frac{\varepsilon_c^{pl}}{\varepsilon_c^{in}} \tag{7}$$

$$G_{fc} = \left(\frac{f_{cm}}{f_{tm}}\right)^2 G_{ft} \tag{8}$$

On the other side, the formula in Equation (9), proposed by Cornelissen [65] and validated by Hordijk [66], was employed in the present study to model the tension behavior of concrete, as shown in Figure 3b, using the STRA option since it gives the best results compared to the others [67]. In this formula, σ_t is the tensile stress normal to the crack direction, f_t is the modified tensile strength determined using Equation (10), w_t represents

the crack opening displacement at any stress level σ_t, w_{cr} is the crack opening displacement at the complete release of the stress or fracture energy obtained using Equation (11) as a function of the fracture energy G_{ft} and the mean tensile strength f_{tm}, and $c_1 = 3.0$ and $c_2 = 6.93$ are constants determined from the tensile tests of concrete [66]. The mean tensile strength f_{tm} and the fracture energy G_{ft} can be obtained from Equations (12) and (13), respectively, following the CEB-FIP model code (2010). In Equation (13), $f_{cmo} = 10$ MPa and G_{fo} is the base fracture energy depending on the maximum aggregate size d_{max}. The value of G_{fo} is selected as 0.028 N/mm for d_{max} equivalent to 12.5 mm used in the tested exterior and interior joints. In this study, a reduction factor of 0.7 is selected for the modified tensile strength f_t to avoid overestimating the tensile softening behavior [68,69]. The descending segment of the tensile stress–strain curve in Figure 3b was obtained in terms of the crack opening from the kinematic relation presented in Equation (14), assuming that there is a single crack per element perpendicular to the tensile stress. In this equation, ε_t and ε_{tm} represent the tensile strain and the strain at the tensile strength, respectively.

$$\frac{\sigma_t}{f_t} = \left[1 + \left(c_1 \frac{w_t}{w_{cr}}\right)^3\right] e^{\left(-c_2 \frac{w_t}{w_{cr}}\right)} - \left[\frac{w_t}{w_{cr}}\left(1 + c_1^3\right)\right] e^{-c_2} \tag{9}$$

$$f_t = 0.7 \sim 1.3 f_{tm} \tag{10}$$

$$w_{cr} = 5.14 \frac{G_{ft}}{f_{tm}} \tag{11}$$

$$f_{tm} = 0.317 (f_{cm})^{0.6} \tag{12}$$

$$G_{ft} = G_{fo} \left(\frac{f_{cm}}{f_{cmo}}\right)^{0.7} \tag{13}$$

$$\varepsilon_t = \varepsilon_{tm} + \frac{w_t}{l_{ch}}, \; \varepsilon_{tm} = \frac{f_t}{E_{cm}} \tag{14}$$

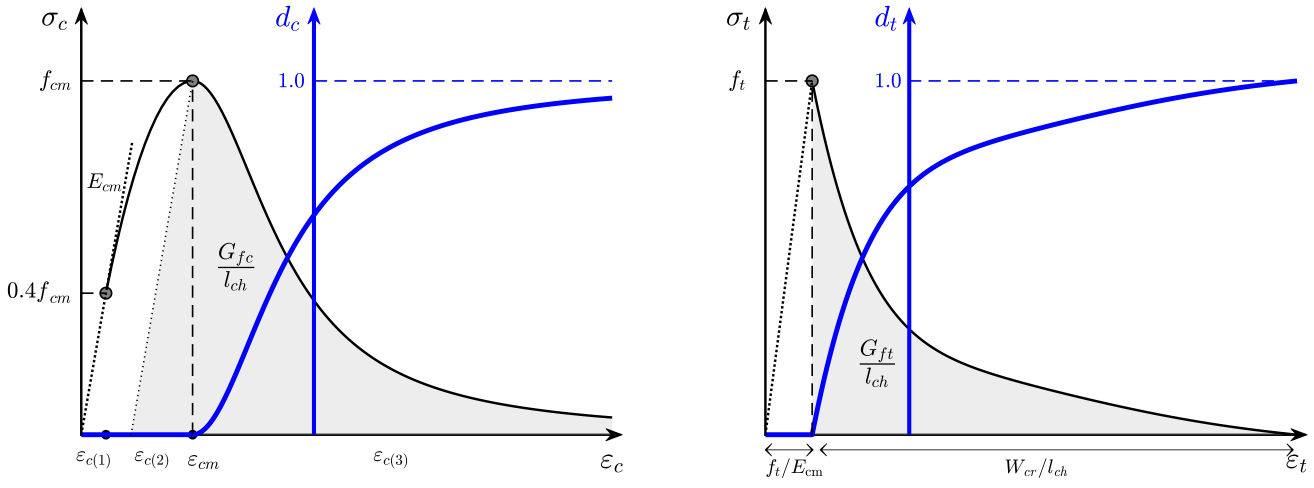

(**a**) (**b**)

Figure 3. Energy-based models for uniaxial behaviors of concrete in (**a**) compression, and (**b**) tension.

For the damage evaluation, the CDP model utilizes the scalar isotropic damage equation. Two independent uniaxial damage variables, d_c and d_t, are used to characterize the responses of the degraded material in compression and tension following

Equations (15) and (16), respectively [70]. Moreover, the values used to establish the curves in Figure 3 are summarized in Table 1.

$$d_c = 1 - \frac{\sigma_c}{f_{cm}} \tag{15}$$

$$d_t = 1 - \frac{\sigma_t}{f_t} \tag{16}$$

Furthermore, the multi-axial behavior in the CDP model is characterized by four parameters, i.e., the tensile-to-compressive meridian ratio K_c, plastic potential eccentricity ϵ, biaxial-to-uniaxial compressive strength ratio $\frac{\sigma_{bo}}{\sigma_{co}}$, and dilatation angle ψ°. CDP parameters have been subjected to some degree of uncertainty due to variations in material properties and testing conditions [35]. However, because ψ°, which is used to define the non-associated potential plastic flow, depends on the confinement pressure and loading history [71], it requires careful calibration to ensure accurate results. To achieve this, K_c, ϵ, and $\frac{\sigma_{bo}}{\sigma_{co}}$ are set to the model's default values, as shown in Table 1. On the other side, a sensitivity analysis has been performed using the values of 52°, 45°, and 56° for ψ°. The capacity loads of the exterior and interior joints converged at 56°. However, the numerical curves achieved the convergence at the cracking and yielding stages when ψ° of the beam was reduced to 48° and 35° for the exterior and interior connections, respectively. This technique provided a good representation of the cracks' growth and distribution, close to laboratory observations. For the parametric study, dilatation angles of 48° for the beam and 56° for the column were used.

Table 1. Parameter values for modeling CDP in the exterior and interior connections.

Ref.	f_{cm} (MPa)	E_c (GPa)	ε_{cm}	ν	f_t (MPa)	G_{ft} (N/mm)	G_{fc} (N/mm)	K_c	ϵ	$\frac{\sigma_{bo}}{\sigma_{co}}$		ψ°
Exterior connection	29.5	23.15	0.0016	0.2	1.7	0.06	4.5	2/3	0.1	1.16	Beam	48
											Column	56
Interior connection	57.0	30.6	0.0017		2.7	0.1	12				Beam	35
											Column	56

3.1.2. Reinforcing Steel

The steel is modeled using isotropic elasticity and von Mises' classical metal plasticity yield surface. The associated plastic flow is determined using the uniaxial stress–strain relationship coupled with damage and failure for ductile metals. The stress in the steel rebars is obtained following Mander [72], as in Equation (17).

$$f_s = \begin{cases} E_s \varepsilon_s & \text{for} \quad \varepsilon_s \le \varepsilon_y \\ f_y & \text{for} \quad \varepsilon_y \le \varepsilon_s \le \varepsilon_{sh} \\ f_y + \left(\frac{\varepsilon_u - \varepsilon_s}{\varepsilon_u - \varepsilon_{sh}}\right)^p (f_y - f_u) & \text{for} \quad \varepsilon_{sh} \le \varepsilon_s \le \varepsilon_u \\ f_u & \text{for} \quad \varepsilon_s \le \varepsilon_F \end{cases} \tag{17}$$

where E_s is the steel's modulus of elasticity, f_y is the yield stress of the reinforcing steel, p is a parameter used to define the hardened part of the steel behavior, which is equal to 4, f_u is the ultimate strength of the reinforcing steel, ε_y is the yield strain where the yield plateau begins, ε_{sh} is the strain where the yield hardening begins, ε_u is the steel strain corresponding to f_u, and ε_F is the steel fracture strain. The properties of the steel rebars used in the exterior and interior eccentric joint specimens W150 and J−10 are listed in Table 2. For the parametric study, the ASTM A706 steel reinforcement is utilized for the longitudinal bars and stirrups.

Table 2. Steel material properties for the exterior and interior joints.

Ref.	Steel Type	Bar Size	E_s (MPa)	f_y (MPa)	ε_y	f_u (MPa)	el %
Exterior connection	ASTM A706 [51]	No. 7 22 mm long bars for beams and columns	200,000	454.5	0.00227	682.4	10
		No. 3 10 mm stirrups for beams and columns	200,000	471.3	0.00236	715.3	12
Interior connection	USD685 [53]	No. 6 19 mm long bars for columns	202,000	746	0.0055	1011	12
		No. 6 19 mm long bars for beams	185,000	710	0.0056	928	12
	SBPD1275/1420 [54]	6.2 mm stirrups for beams and columns	199,000	1276	0.0077	1453	5

E_s is the elastic modulus of the steel reinforcing bars, f_y is the yield stress, ε_y is the yield strain, f_u is the ultimate stress, and el% is the elongation of the reinforcing bars.

3.1.3. Bond between Concrete and Steel

The bond-slip between the concrete and reinforcing bars plays an essential role in the beam–column joint's structural behavior, including shear capacity, ductility, and crack propagation [73]. Several techniques exist to simulate the interface contact between the concrete and the reinforcing bars, depending on how the bars are modeled (i.e., continuum solid or structural element). For modeling reinforcing bars as structural elements, the bond-slip behavior can be explicitly modeled via local bond-slip behavior using spring-like contact elements, known as translators, where the interface elements are restrained in the transverse direction and only allowed to move in the rebar direction simulating the slip conditions. The bond-slip relationships for the exterior and interior joints are shown in Figure 4a,b. Zone one and zone two are divided based on the differences in the bond-slip relationships between the concrete and the reinforcing bars within and outside the column of the joint. Zone one extends from the column face to a distance equal to a beam depth from the column face. Zone two is the joint zone within the column. Two different translator types are modeled. The translator for zone one is defined by the bond strength τ, while the translator for zone two is defined via $\Omega_{p,tr}\tau$. $\Omega_{p,tr}$ accounts for the improvements resulting from the column axial force, while other factors that might impact the bond strength are implicitly modeled through tension-softening behavior. The bond–slip constitutive relationship is assumed following the CEB–FIP model (2010). In the model, the local bond stress τ is computed as a function of the relative slip s, as in Equation (18):

$$\tau = \begin{cases} \tau_{max}(s/s_1)^{\alpha} & \text{for} \quad 0 \le s \le s_1 \\ \tau_{max} & \text{for} \quad s_1 < s \le s_2 \\ \tau_{max}(\tau_{max} - \tau_f)\frac{(s-s_2)}{(s_3-s_2)} & \text{for} \quad s_2 < s \le s_3 \\ \tau_u & \text{for} \quad s_3 < s \end{cases} \tag{18}$$

where $\tau_{max} = 2.5\sqrt{f_{cm}}$ is the maximum bond strength, and $\tau_f = 0.4\tau_{max}$ is the transferred bond stress by friction, which demolishes at a slip value of 40 × the bar diameter (40D) [74]. The relative slip limits s_1 and s_2 are selected as 1 mm and 2 mm, respectively. On the other hand, s_3 is assumed as the clear distance between the rebar ribs c_{clear}, which is equal to 11 mm for the exterior joint and 9 mm for the interior joint. The bond forces for the translator elements for zone one, $F_{Translator_1}$, are computed using Equation (19) as:

$$F_{Translator_1} = \tau.l.\pi.D \tag{19}$$

where l is the spacing between the translator elements is equal to 25.0 mm, and D is the diameter of the bar. For zone two (joint zone), Equation (19) is modified by the increase factor $\Omega_{p,tr}$, which is obtained using Equation (20) [55] as:

$$\Omega_{p,tr} = 1.0 - tanh\left(0.2\frac{P_{tr}}{0.1f_{cm}}\right) \tag{20}$$

where P_{tr} is the transverse compression force. The translator forces in zone two can be, therefore, obtained using Equation (21) as:

$$F_{Translator_2} = \Omega_{p,tr}.F_{Translator_1} \quad (21)$$

For computational efficiency, a full bond is assumed in the remaining regions of the model since these regions are less susceptible to observing debonding between steel rebars and concrete. The full bond is achieved by utilizing the embedded constraint algorithm between the embedded element (steel parts) and the host element (concrete parts).

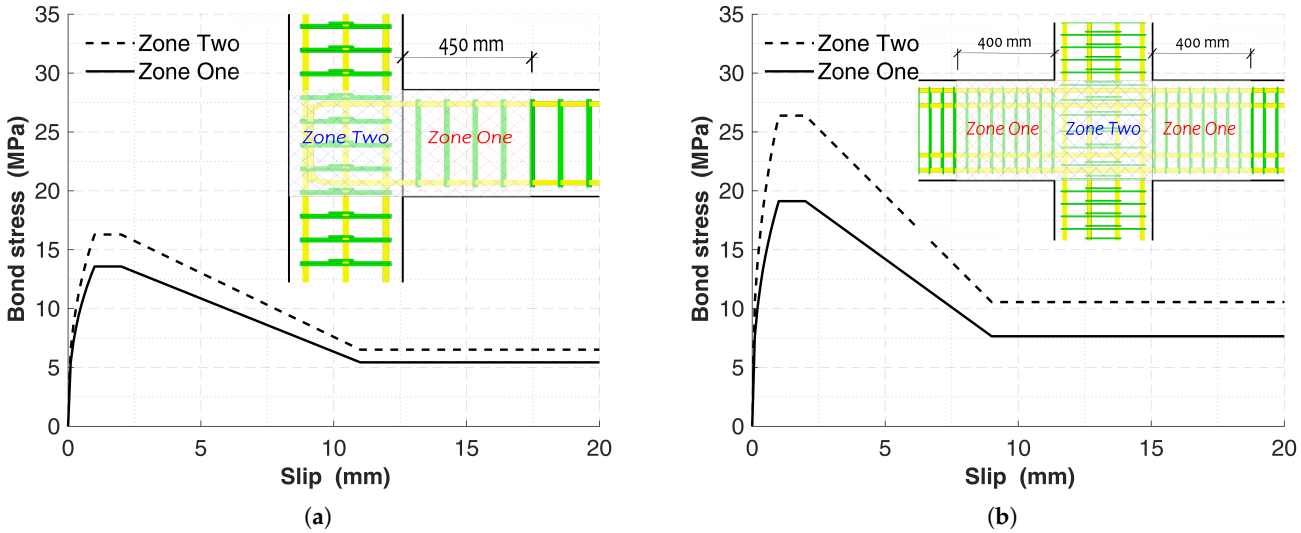

Figure 4. Bond behavior models adopted in ABAQUS for the eccentric joints implemented with the translator elements: (**a**) exterior joint, and (**b**) interior joint.

3.2. Meshing

Incompatible mesh element C3D8I is used to define the concrete elements over other types of first-order interpolation hexahedral elements (i.e., full C3D8 and reduced C3D8R integration elements) to avoid shear locking and hourglass effects via its extra shape functions [43,75–82]. On the other hand, the steel reinforcement was modeled as discrete structural elements. The stirrups were modeled using the T3D2 truss mesh element type, while the longitudinal bars were modeled using the B31 beam mesh element type to enable rebar compressibility [43]. In addition to the steel material's Poisson's ratio of 0.3 utilized with the truss and beam mesh types, a Poisson's ratio of 0.5 [31] was used in defining the longitudinal bars section.

For the FEM, the element size is selected to satisfy two conditions. First, according to crack band theory, the mesh element size must be in the range of the characteristic length of concrete introduced by Hillerborg et al. [83]. The characteristic length of concrete, also known as the crack band width, represents the part of the crack where the stress transfer is possible, which ranges between d_a to $6d_a$, where d_a is the nominal size of the concrete aggregate [84]. Others developed Equation (22) based on the modulus of elasticity, fracture energy, and main tensile strength to compute the characteristic length of concrete [83]. However, Bažant and Pijaudier-Cabot [85] reported the concrete characteristic length experimentally to be equal $3d_a$. Recently, it has been statistically calculated from many experiments, which have found it to be equal to 26 mm [86]. Second, in order to simulate the stiffening behavior between steel and concrete, the mesh element size must be greater than the magnitude computed from Equation (23) [87]. In the equations, α_{ts} and $\rho_{s,ef}$ represent the strength level of the interaction stress contribution, ranging between 0.4 and 1.0, and the effective reinforcement ratio, respectively. Based on the aggregate size of 12.5 mm that was used for both experimental reference joints, an element size of 25 mm was selected.

$$h < \frac{E_c\, G_{ft}}{f_{tm}^2} \tag{22}$$

$$h > \frac{2G_{ft}}{f_{tm}(\varepsilon_y - \frac{\alpha_{ts}\, f_{tm}}{\rho_{s,ef}\, E_s})} \tag{23}$$

3.3. Boundary Conditions and Simulation Parameters

The ABAQUS\Explicit solver is used to perform the analysis of both joints. The explicit solver was selected over the implicit solver because of its capability to handle problems involving material and geometrical nonlinearities in addition to material damage. The explicit solver uses a time increment close to the stability time $\Delta t = L^e/C_d$ of the model based on the smallest element characteristic length L^e and its material dilatational wave speed $C_d = \sqrt{E/\rho}$, where E is the modulus of elasticity and ρ is the material density, making the computation time related linearly with the load rate scaling factor and the square root of the mass scaling factor.

The tips of the columns and beams were restrained to mimic pin- and roller-supports, confirming full restraint against the torsion moments about the members' axes for both exterior and interior joints through implementing kinematic-coupling constraints, as shown in Figure 5a,b. The axial column load was applied at the beginning of the simulation via a load-controlled step and held constant throughout the simulation time. The lateral displacements were further applied monotonically at the beams' tips. The analysis was carried out using double-precision accuracy through the built-in smooth-step amplitude curve, as shown in Figure 6, to suppress the dynamic oscillation with a velocity of 400 mm/s, similar to those utilized by Thai et al. [88] and Thai and Uy [89], resulting in a small friction of kinematic energy equal to 2% of the internal energy. However, a fixed mass scaling factor was employed to modify the stability time since it reduced significantly through the analysis because of damage and/or plasticity.

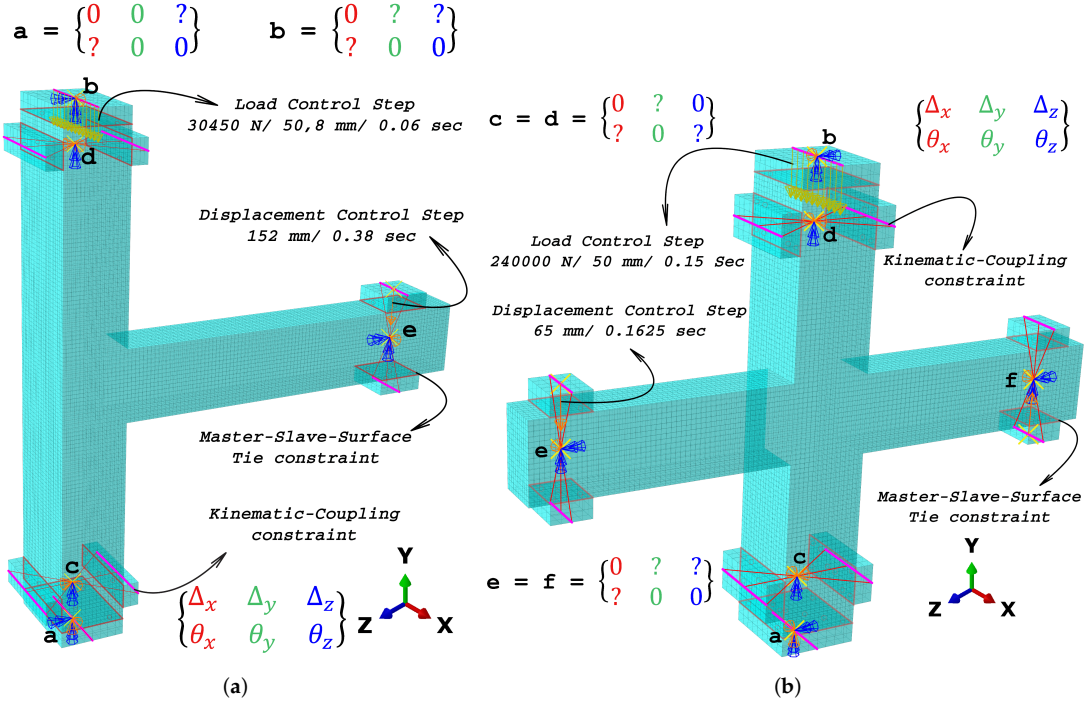

Figure 5. Loads, constraints, and boundary conditions for the eccentric joint models: (**a**) exterior joint, and (**b**) interior joint.

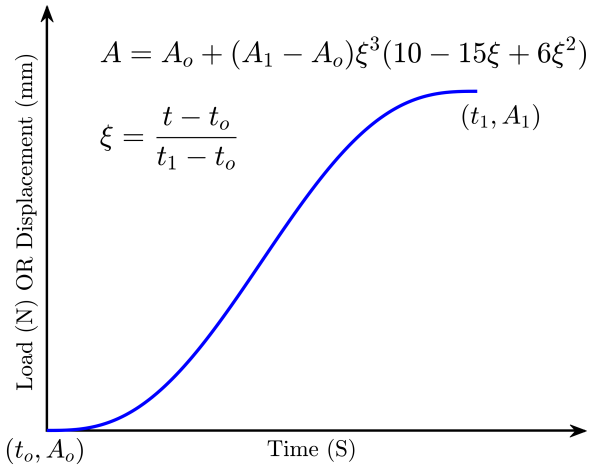

Figure 6. Smooth-step amplitude definition used to implement the load- or displacement-control steps.

4. Parametric Study

The geometric configurations of the beam–column joint have the most significant influence on its behavior after the material strength [4]. Hence, a parametric study was carried out on the geometric parameters of eccentric beam–column joints using the previously calibrated FE configurations. The study matrix consisted of three parameters: the joint type (interior and exterior joints), the joint aspect ratio (the ratio of the beam depth to column depth), and the column aspect ratio, as listed in Table 3. The cross-section dimensions, reinforcement details, and model properties are all featured in Figure 7. Notably, b_c stands for the column width, while d_c and d_b refer to the depths of the column's and beam's cross-sections, respectively, and e is the eccentricity. Symmetrical reinforcement was utilized on both the top and bottom of the beams, whereas the columns were modeled with a reinforcement ratio of 1.8%. The ranges for the examined geometrical parameters were selected within the limits of ACI-318 [27].

Table 3. The matrix of the current beam–column joint study.

Beam Dimensions (mm)	Joint Type	Column Dimensions (mm)	Eccentricity (e/b_c)	Joint Aspect Ratios (d_b/d_c)	Column Aspect Ratios (b_c/d_c)
450 × 300	Interior	600 × 400	0.25	1.125	1.5
		800 × 400	0.3125		2.0
		1000 × 400	0.35		2.5
	Exterior	600 × 400	0.25		1.5
		800 × 400	0.3125		2.0
		1000 × 400	0.35		2.5
600 × 300	Interior	600 × 400	0.25	1.5	1.5
		800 × 400	0.3125		2.0
		1000 × 400	0.35		2.5
	Exterior	600 × 400	0.25		1.5
		800 × 400	0.3125		2.0
		1000 × 400	0.35		2.5
800 × 300	Interior	600 × 400	0.25	2.0	1.5
		800 × 400	0.3125		2.0
		1000 × 400	0.35		2.5
	Exterior	600 × 400	0.25		1.5
		800 × 400	0.312		2.0
		1000 × 400	0.35		2.5

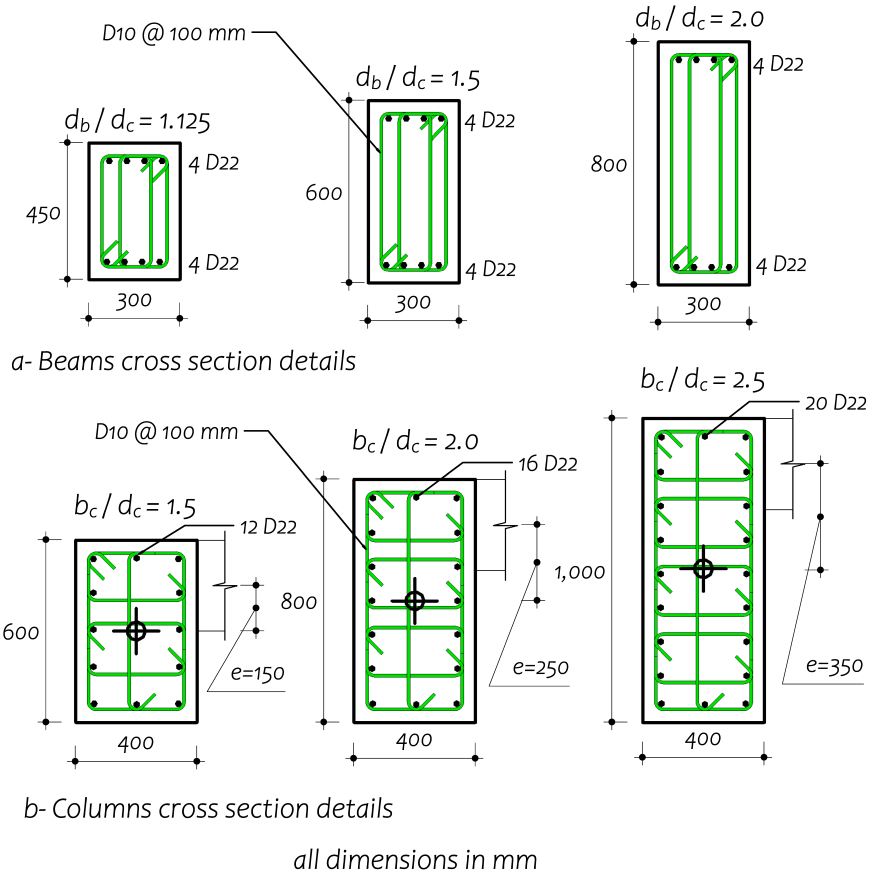

Figure 7. Dimensions of cross-sections and their reinforcement details for the models used in the parametric analysis.

5. Results and Discussion

5.1. FE Model Calibration

The accuracy of the nonlinear finite element model using the previously calibrated constitutive model parameters and discretization characteristics is evaluated by comparing the numerical outputs with the experimental results in terms of the global and local behaviors of the joint subassemblies, the cracking pattern, failure mode, and strain profile of the steel reinforcement. In the case of the experiments, the joints were subjected to reversed cyclic loading, and hence, the force–deformation responses in the global and local behaviors are presented by the hysteresis loops. On the other hand, the FE model produced the force–deformation relationship in the form of backbone curves. The validation aims to ensure that the numerical models can predict the experimental behavior of the joints as closely as possible.

5.1.1. Global Behavior

The global behaviors of the exterior and interior joints are shown in Figure 8a,b, respectively. The figures show that the damaged plasticity model with the calibrated parameters can successfully predict the different failure mechanisms for both joints. However, the predicted curve for the exterior joint (W150) was slightly overestimated at the yield point, by about 3%, which can be considered negligible. Moreover, although the predicted and experimental readings for the maximum load points were almost identical, the predicted one was observed at a 4.5% drift ratio (DR), while it was located at 4.0% DR for the experimental specimen. This is acceptable since the maximum capacity of the joint is the point of intersection between the beam input shear and the joint shear capacity curves, which is

positioned between two load cycles. On the other hand, the predicted interior joint curve is consistent with the experimental one.

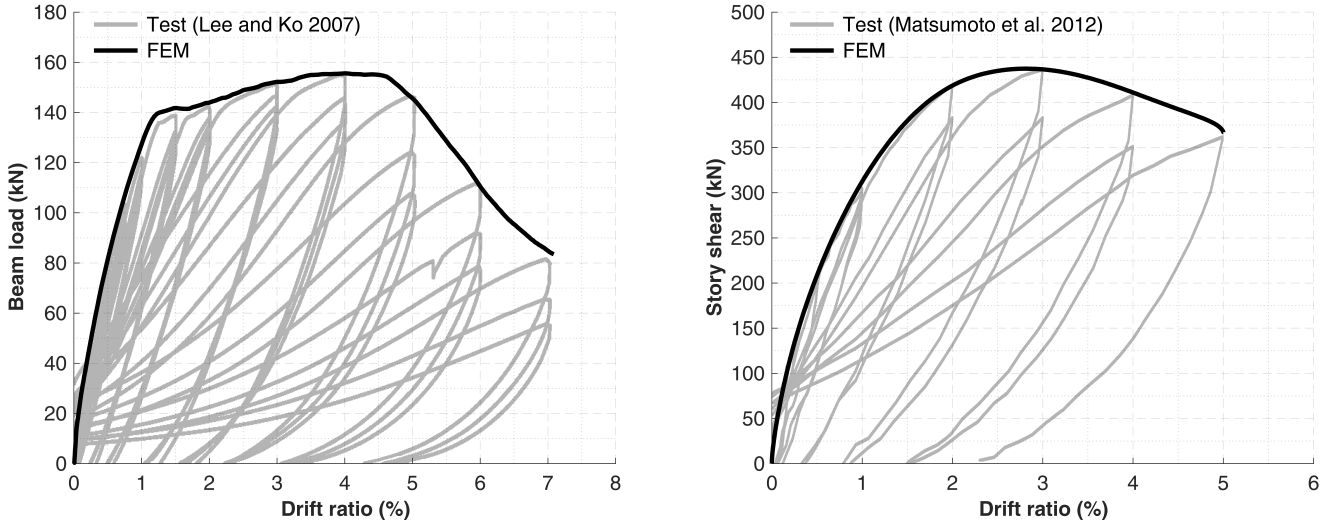

(**a**) (**b**)

Figure 8. Global behaviors of the eccentric joint subassemblies: (**a**) exterior joint [16], and (**b**) interior joint [14].

5.1.2. Local Behavior

The local behaviors of the joints, involving the forces, moments, and deformations obtained via the integrated variables through the interior cross–section surfaces method, were compared to the laboratory measurements. Figure 9 reveals that the implemented previous method in the FE model can capture the real beam moment–rotations measured at two different locations on the beam of the exterior joint (W150) [16]. On the other side, the predicted joint shear behavior, defined as the joint shear force derived from the preceding technique versus the average of the shear distortions of the mesh elements located in the beam and column intersection, converges to the experimental readings with acceptable accuracy, as shown in Figure 10a,b.

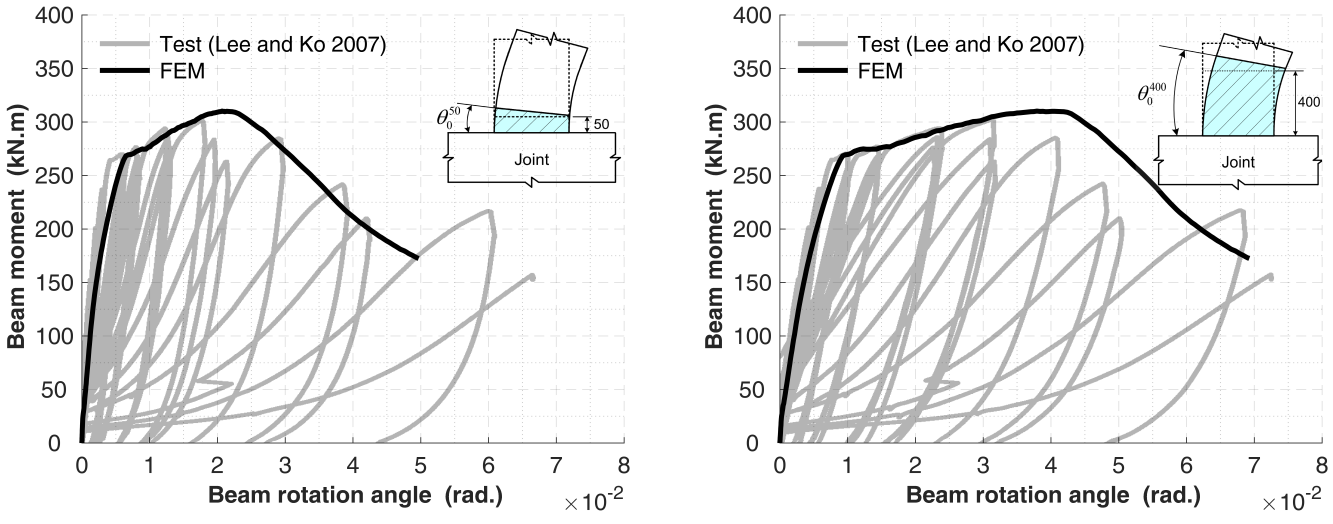

(**a**) (**b**)

Figure 9. Comparisons between the measured beam behaviors for the experimental test [16] and calibrated model of the eccentric exterior joint subassemblies.

The cracking of the exterior and interior joints was initiated at 254 kN and 640 kN associated with shear distortion angles of 2×10^{-4} rad and 8×10^{-4} rad. Furthermore, the shear capacities for the exterior and interior joints reached about 750 kN and 1954 kN at shear distortion angles of 0.0075 rad and 0.024 rad. At the maximum load, the exterior joint zone was found to resist shear forces six times that of the column, while this value was about four and a half for the interior joint. This agreed with the findings of Paulay [90], that the joint area is subjected to around four to six times the column shear force. Nonetheless, the main reinforcing steel was found to resist about 6% of the joint shear force for the interior joint through the reinforcement dowel action and less than 2% for the exterior joint.

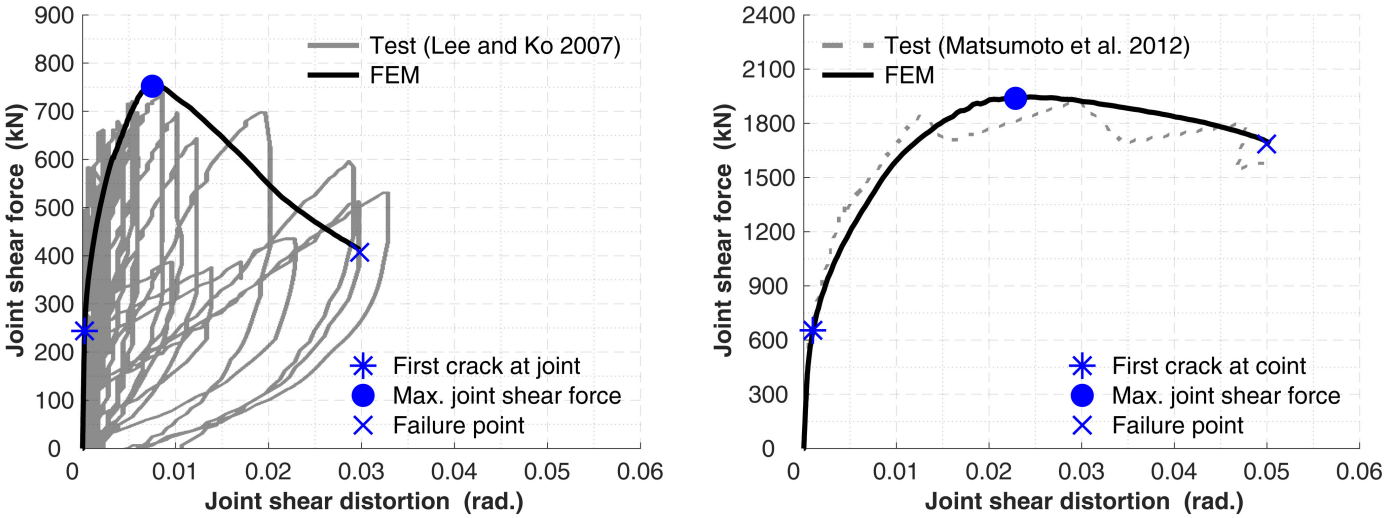

Figure 10. Local behaviors (joint shear force vs. joint shear distortion angle) for the eccentric joints: (**a**) exterior joint [16], and (**b**) interior joint [14].

5.1.3. Cracking Pattern

Observing cracking patterns is a cornerstone in assessing the responses of reinforced concrete elements. Since the CDP model does not provide the material cracks, the crack pattern was graphically assessed by examining the contour plots of the maximum principal plastic strain PE. Figures 11 and 12 display the comparisons between the predicted and experimental results of the cracking patterns of the eccentric exterior and interior joint models, respectively, at the end of the test. The flush sides of the joints experienced extensive diagonal shear cracks, which initiated at 0.25% DR and 0.5% DR for the exterior and interior joints, respectively. Later, new cracks grew until the maximum point load, and they expanded rapidly, resulting in concrete spalling at the joint faces, as shown in Figures 11a and 12a. Although the far side of the exterior joint had no cracks, vertical hair cracks developed on the far side of the interior joint, as shown in Figure 12b, which may be attributed to the effect of the intermediate level $(0.2A_g f_{cm})$ of the column axial load [91]. Moreover, the columns of both joints suffer from flexural and torsional cracks resulting from the joint eccentricity, in addition to a concrete spalling due to the bent bar pushing of the beam for the exterior joint model. Moreover, flexural cracks were initiated at around 1.0% DR for both joints, while the torsional cracks developed at a 2% DR. Furthermore, the cracks of the beam for the interior joint subassembly exhibited uneven depth and width between the beam faces due to the out-of-plane moment, which reached 16% of the in-plane flexure moment. However, this percentage was only 4% for the exterior joint.

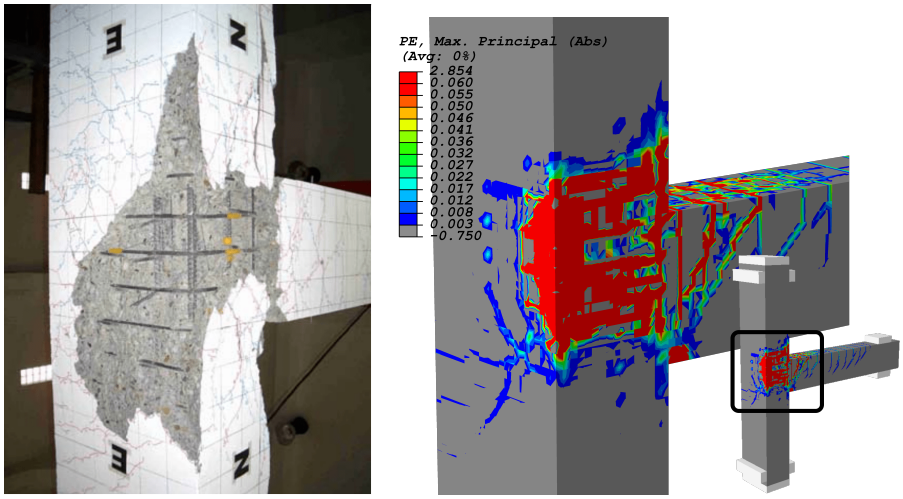

(**a**)

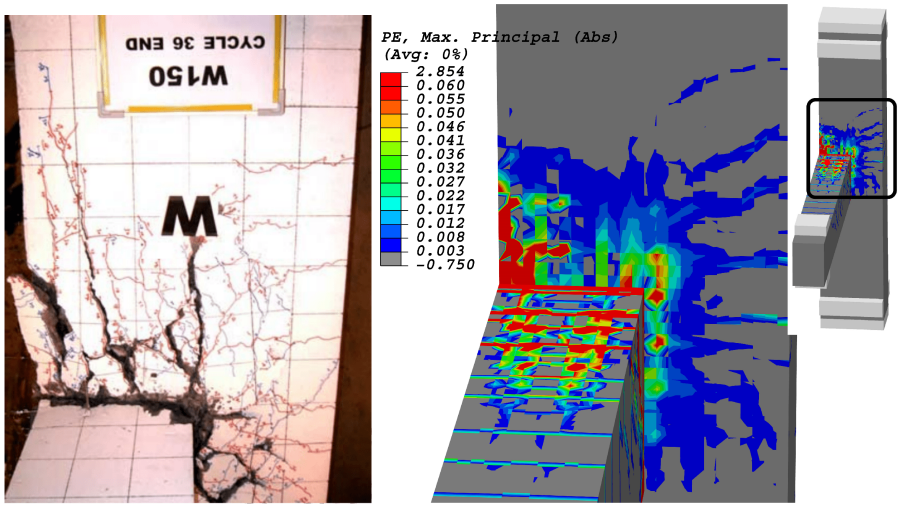

(**b**)

Figure 11. Comparisons of the cracking patterns between the experiment [16] and the FE model for the eccentric exterior joint: (**a**) flush side, and (**b**) beam-to-column interface.

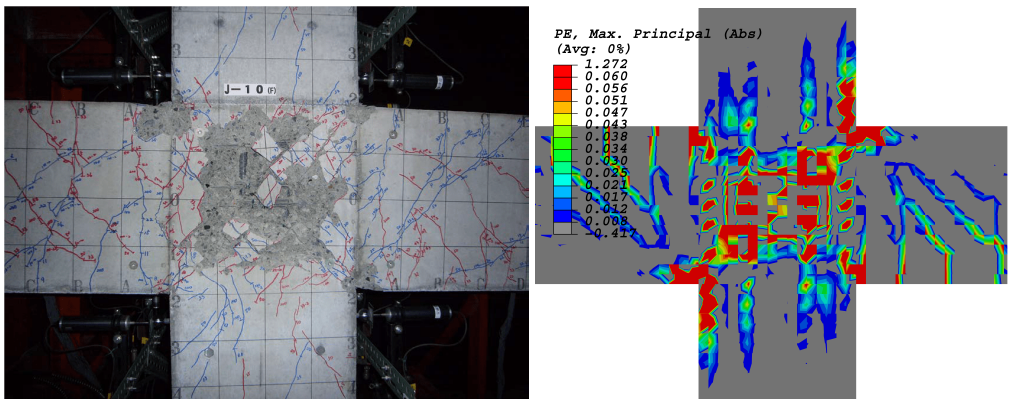

(**a**)

Figure 12. *Cont.*

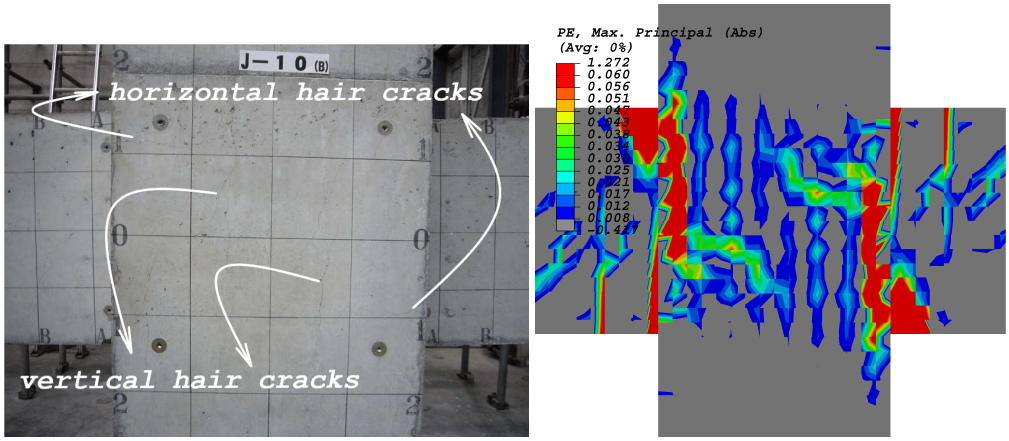

(**b**)

Figure 12. Comparisons of the cracking patterns between the experiment [14] and the FE model for the eccentric interior joint: (**a**) flush side, and (**b**) far side.

5.1.4. Strains in Steel Rebars

The numerical outputs of logarithmic strain LE11 in Figure 13 show a good agreement with the laboratory measurements reported in [16]. To this end, Figure 14a,b show the plastic strain PE11 of the steel reinforcement for both models. The beam bars yielded for both joints unsymmetrically due to the out-of-plane beam moment. The yielding extended 750 mm and 250 mm away from the column face for the exterior and interior joints, respectively. On the other side, the joint stirrups began to yield after the maximum load since the strain in the inner stirrup legs increased as the joint cracking increased, suggesting its vital role at this stage. These findings align with the research by Hwang et al. [92], which suggests that joint stirrups primarily delay joint collapse by controlling cracking rather than increasing shear strength through confinement.

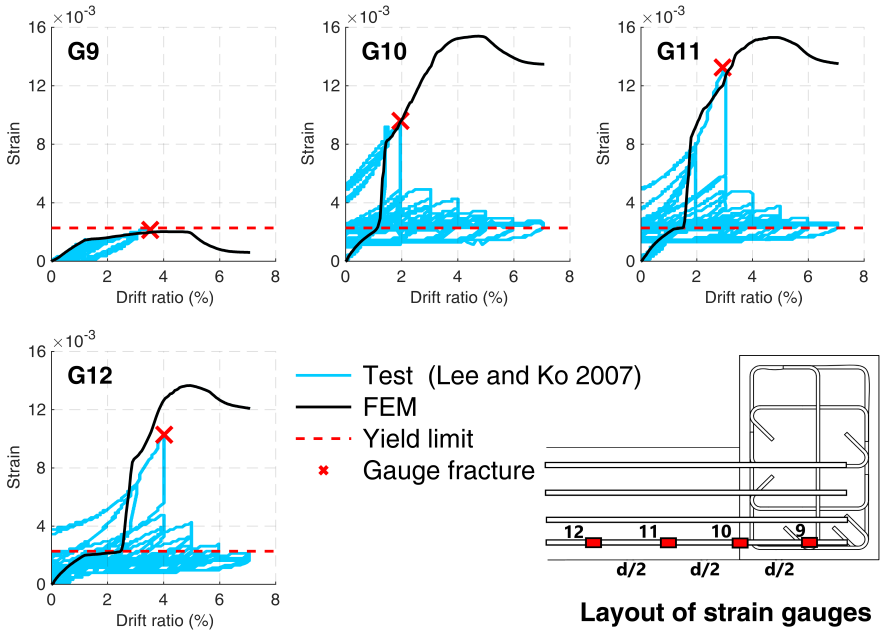

Figure 13. Comparison between the numerical outputs and the experimental gauge readings for the exterior joint [16].

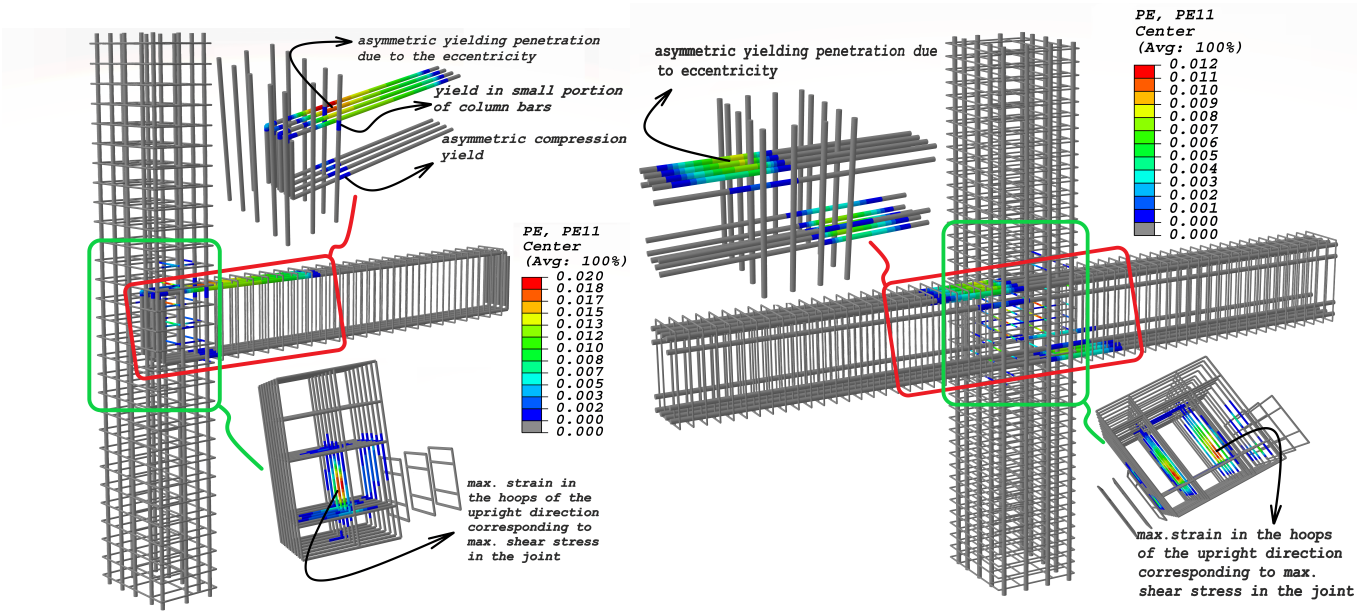

Figure 14. Plastic strains (PE) detecting the reinforcement yielding of the eccentric joint subassemblies at the end of the test: (**a**) exterior joint subassembly, and (**b**) interior joint subassembly.

5.2. Parametric Study

The effect of the geometrical parameters on the beam–column joints was assessed by investigating the global behavior, which involves observing the beam load vs. drift ratio, and local behaviors, which involves investigating joint shear force vs. joint shear distortion and joint torsional moment vs. joint twist angle. The cracking pattern of the joints was also investigated to assess the failure behavior.

5.2.1. Global Behavior

Figure 15 depicts the performances of both types of joints (exterior and interior) with a constant column aspect ratio of 1.5 and various joint aspect ratios of 1.125, 1.5, and 2.0. Figure 15a shows that the interior joint collapsed earlier at 6.5% DR compared to the exterior joint, which failed at 7% DR for a 1.125 joint aspect ratio. However, the collapse becomes faster as the joint aspect ratio increases for both joints. It happens at 6.0% DR and 4.75% DR for the joint aspect ratios of 1.5 and 2.0, respectively. The failure point is obtained by observing the kinetic energy profile of the model [93]. Moreover, the post-peak segment of the interior joints became steeper as the joint aspect ratio increased. This can likely be attributed to the out-of-plane moment of the beams [1,11], as shown in Figure 15b, that reaches around 14.5%, on average, of the in-plane flexural moment measured at the same section, resulting in a decrease in the joint panel confinement by the beams [94]. Overall, the interior joints have inferior performances, with the maximum loads lower by 25% than the exterior ones. Figure 16 also depicts the effect of changing the column aspect ratio, with values of 1.5, 2.0, and 2.5, while maintaining a constant joint aspect ratio of 1.125. Figure 16a shows that changing the column aspect ratio can lead to a modest improvement of less than 5% on the max load for the interior joints, while it improves the exterior joints ability to resist the load beyond a 6% DR. Moreover, it was found that the accelerated decrease in the load after 4% DR for the interior joint with column aspect ratios of 2.0 and 2.5 is related to the change in the rotation of the right beam of the joint subassembly, as shown in Figure 16b.

Figures 15a and 16a reveal that the interior joints initiate cracking at half the beam load and drift ratio of the exterior joints. Furthermore, the maximum loads of the exterior joints correlate with the joint stirrups yielding. In contrast, the interior joints experience simultaneous yielding of beam bars and joint stirrups, which is related to their failure type.

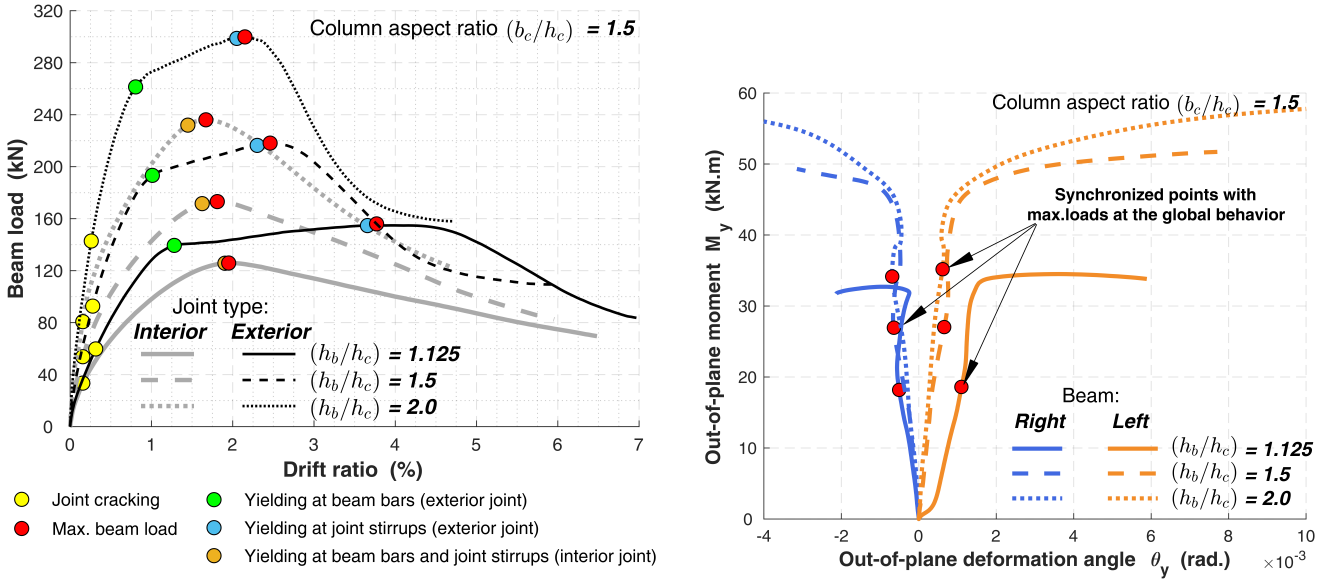

(**a**) (**b**)

Figure 15. Joint aspect ratio impact on the eccentric joint subassemblies: (**a**) beam load–displacement curves for both types of joints (global behavior), and (**b**) moment–rotation behaviors for the right and left beams of the interior joints measured at a distance of 50 mm from the column face.

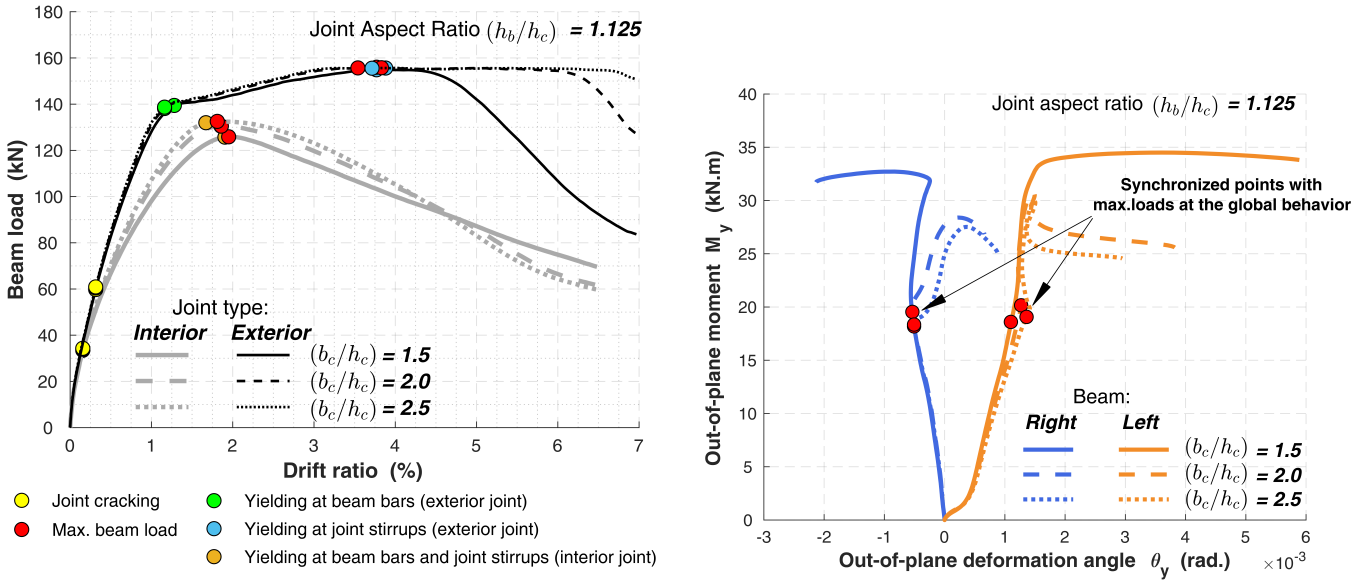

(**a**) (**b**)

Figure 16. Column aspect ratio impact on the eccentric joint subassemblies: (**a**) beam load–displacement curves for both types of joints (global behavior), and (**b**) moment–rotation behaviors for the right and left beams of the interior joints measured at a distance of 50 mm from the column face.

On the other side, Figure 17a shows the characteristics of the backbone behavior curve obtained by the equivalent elasto-plastic energy criteria [95] to calculate the ductility ratio $\mu = \frac{\delta_{p_y}}{\delta_{p_u}}$, where δ_{p_y} is the drift ratio at the yield load P_y and δ_{p_u} is the drift ratio at the load of $0.85P_{max}$. The joint aspect ratio, as shown in Figure 17b, has a predominant impact on the exterior eccentric beam–column joints. The ductility loses more than 20%, increasing the joint aspect ratio from 1.125 to 1.5 and 2.0. However, the interior joints preserved an average ductility of about 3.2 for all joint aspect ratios. On the other hand, the column aspect ratio enhances the ductility depending on the joint type and joint aspect ratio. The exterior joints

with a joint aspect ratio of 1.125 have the best performance, with a ductility ratio reaching 5.8 when the column aspect ratio increases to 2.5; this effect decreases with the increase in the joint aspect ratio.

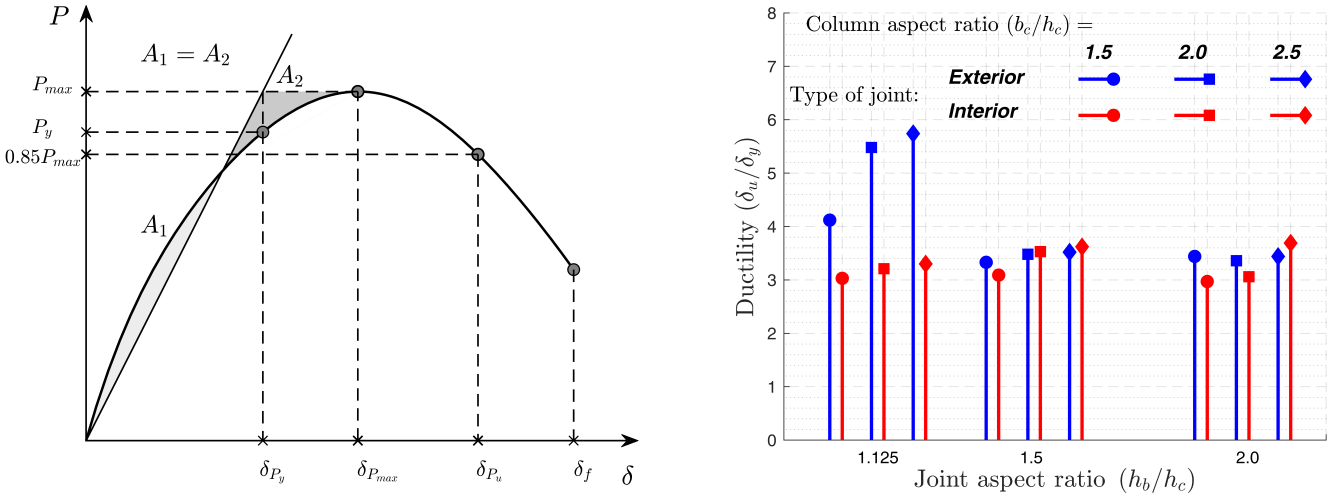

(**a**) (**b**)

Figure 17. Effects of the geometric parameters of the joints on the ductility: (**a**) ductility components definition, and (**b**) computed ductility factor for the models.

5.2.2. Local Behaviors

Figure 18a,b show the torsional behavior of the eccentric joints with the increasing aspect ratios of the joint and column, respectively. The torsional moment at joint cracking does not affect so much by increasing the joint aspect ratio, which is about 35/kNm, on average, as shown in Figure 18a. In contrast, it increases proportionally to the column aspect ratio, as shown in Figure 18b. Furthermore, the maximum torsional moment is directly related to the joint stirrups yielding in the exterior joints and with the simultaneous yielding of the beam bars and joint stirrups for the interior joints.

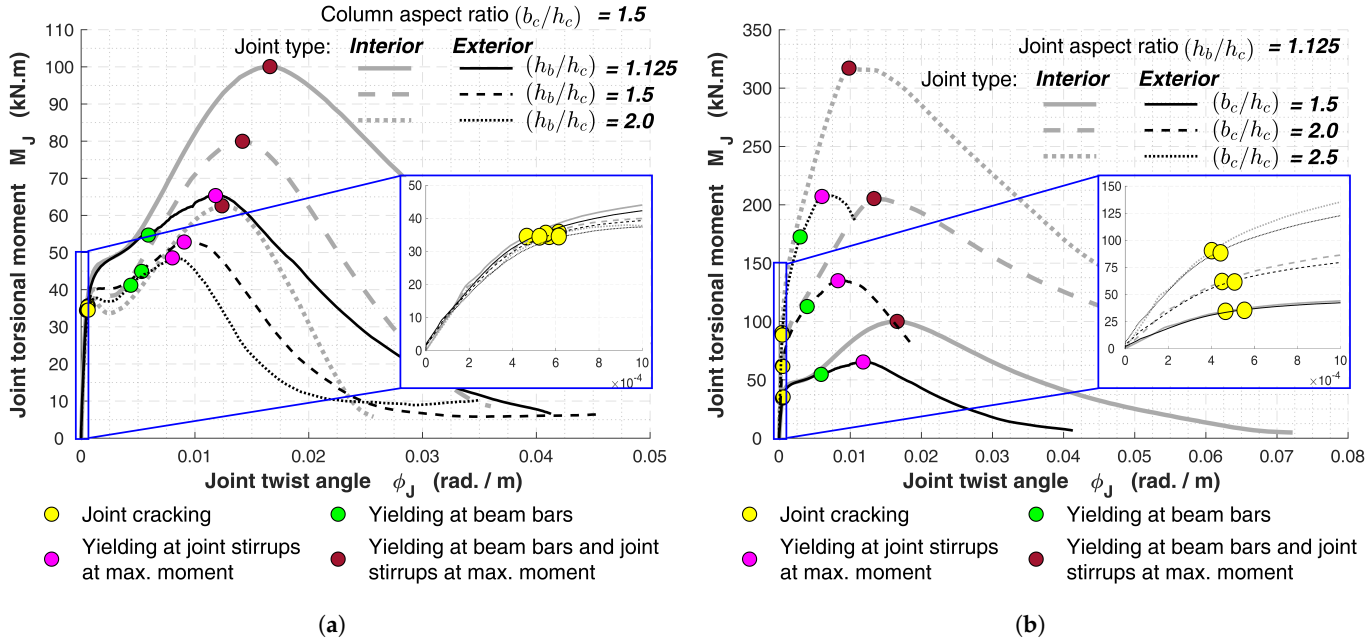

(**a**) (**b**)

Figure 18. The influences of the geometric parameters on the joint torsional behavior curves for both types of joints: (**a**) joint aspect ratio impact, and (**b**) column aspect ratio impact.

Figure 19 compares the joint torsional moment capacities and their corresponding rotational angles. The joint rotational angle is computed as the summation of the joint panel's upper and lower torsional angles over its length. Figure 19 shows that the exterior joints resist 68% and 63% of the torsional moment and rotational angle of the interior joints, respectively. Moreover, the torsional moment capacities for the models with the column aspect ratios of 2.0 and 2.5 are about 215% and 335% for 1.5. The capacities, on the other hand, are reduced by 15%, on average, by increasing the joint aspect ratios. Both aspect ratios have the same impact on the rotational angle since they both reduce it by 18%, on average, as they increase, as shown in Figure 19b.

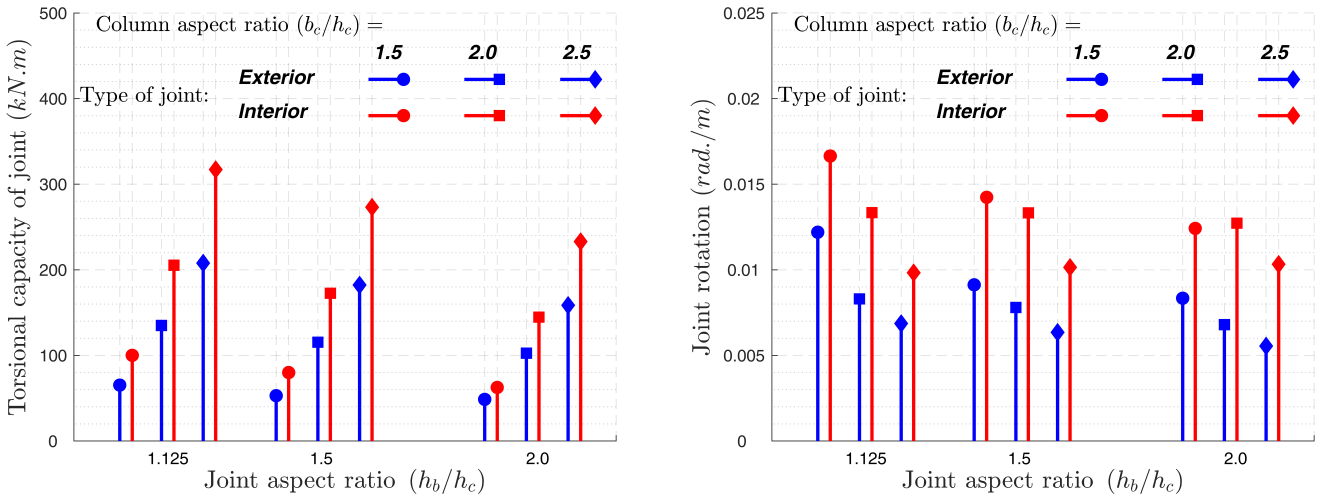

(**a**) (**b**)

Figure 19. Variations in the torsional moments and associated rotational angles with changes in the joint and column aspect ratios for both types of joints: (**a**) joint torsional capacity, and (**b**) joint twist angle.

Figure 20a,b show the shear behavior of the eccentric joints with points that clarify the significant change in the behavior with their related observations when the joint and column aspect ratios increase, respectively. The joint cracking triggers the first stiffness changing at the shear angle of around 2.2×10^{-4} rad, where the corresponding shear forces of the exterior joints are about 93% of those for the interior joints. The concrete began crashing in the joint zone at the maximum joint shear force after developing the theoretical beam yielding capacity for the exterior joints, referred to as BJ failure, followed by the joint stirrups yielding. In contrast, the beam bars and joint stirrups simultaneously yielded for the interior joint without developing the beam yielding capacity, referred to as J failure, especially with the increase in the joint aspect ratio, as shown in Figure 20a. Nevertheless, the increase in the column aspect ratio improves the interior joints to develop the beam yielding capacity, as shown in Figure 20b, and slows down the exterior joint distortion after the maximum shear force. The same observations have been reported by Kim and LaFave [4,96,97], who demonstrated that beam–column joints have distinct changes at key points in their behaviors caused by joint cracking initiation, yielding at beam bars or joint stirrups, and maximum shear force, where the joint begins to lose its resistance. However, a change occurs in the shear behavior for the interior joints with the column aspect ratios of 2.0 and 2.5 after the maximum shear force, as shown in Figure 20b, related to the beam out-of-plane deformation, which triggers a sudden decrease in the joint confinement. Moreover, it was found that the capacity points of the shear force and torsional moment behaviors are not synchronized.

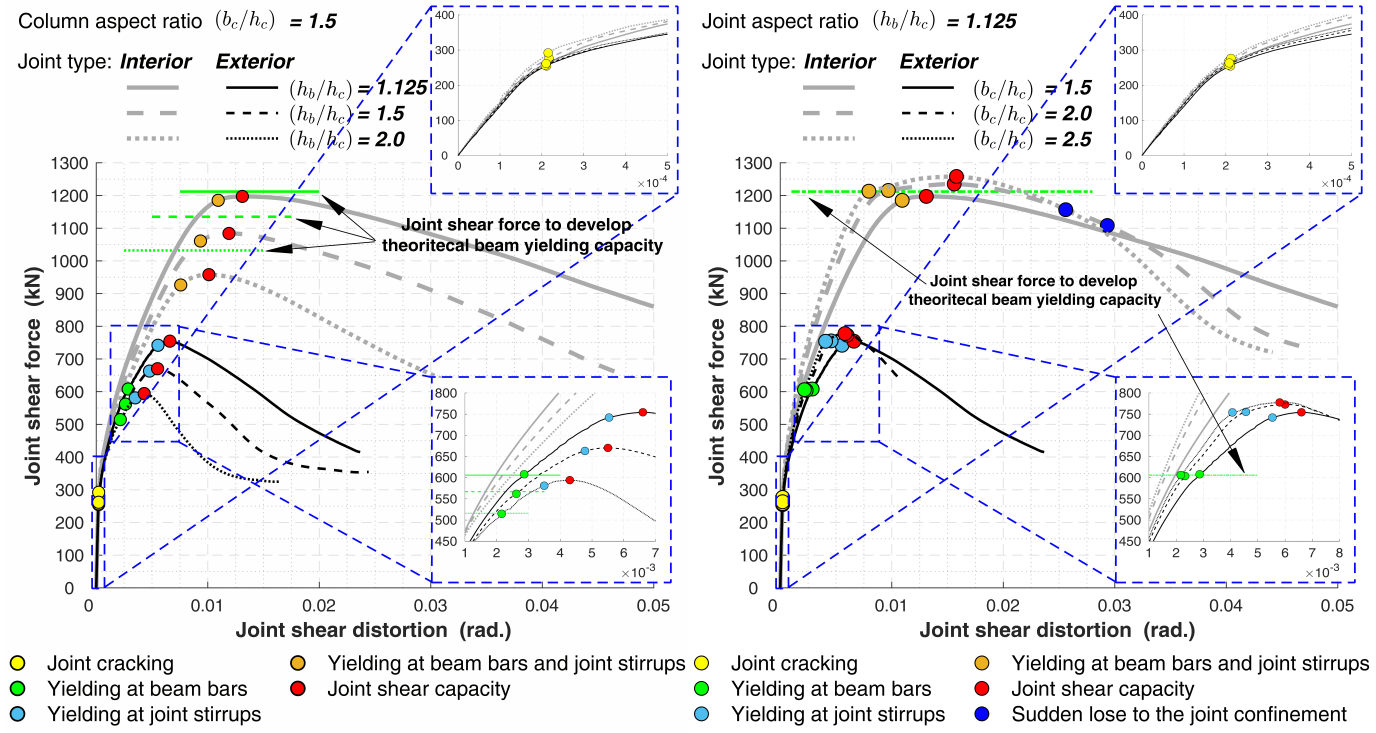

(**a**) (**b**)

Figure 20. The influences of the geometrical parameters on the joint shear behavior curves for both types of joints: (**a**) joint aspect ratio impact, and (**b**) column aspect ratio impact.

Furthermore, Figure 21 compares the joint shear capacities and the corresponding shear distortion angles. The exterior joints sustain a shear force of about 62% of that for the interior joints, which is close to what was reported by Kim and LaFave [4,97] and less than 50% for the corresponding shear distortion angles. As the joint aspect ratio increases, on the other side, the shear capacities decrease by around 10%, and the joint distortion angle reduces by 8% and 26% for the aspect ratios of 1.5 and 2.0, respectively. Despite only modest enhancements in the shear capacities, of less than 5%, due to the increase in the column aspect ratio, the joints are improved, behaving in a ductile manner. Moreover, the shear distortion angles increase by 8%, on average, for the interior joints and decrease by 11% for the exterior joints.

The shear stress coefficient $\gamma = V_j/\sqrt{f_c}$, on the other hand, is used to consider the joint geometrical shape in calculating the joint shear strength V_j as a function of the number of confined joint faces. According to ACI-318 and ACI-352, it is taken as 1.25 for the interior joints, while it is reduced to 1.0 for the exterior joints. Unlike the interior joints, as shown in Figure 21a, the shear stress coefficient overestimates the shear strengths of the exterior joints, especially as the joint aspect ratio increases to a value of more than 1.0, as detected before by Kim and LaFave [97].

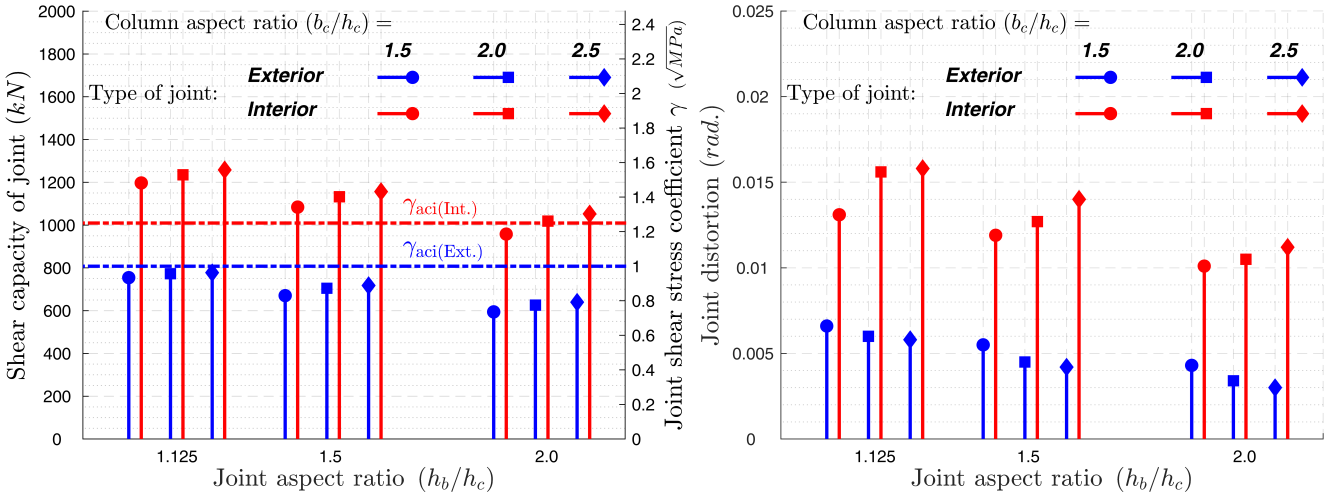

(**a**) (**b**)

Figure 21. Variations in the joint shear capacities and associated shear distortions with the changes in the joint and column aspect ratios for both types of joints: (**a**) joint shear force capacity, and (**b**) joint shear distortion.

5.2.3. Crack Assessment

The plastic strain contours at the maximum load in the global behavior for the joint models have been used in assessing the effect of the geometrical parameters on the behavior of the cracking pattern. Figure 22 depicts the differences in the cracking patterns between the exterior and interior joint models. The damage is concentrated in the beam for the exterior joint, as shown in Figure 22a, since the joint failure occurs after the beam plastic hinge has been developed. On the other hand, the damage is concentrated at the joint zone for the interior joint model that failed before the beam reached its yielding capacity, as shown in Figure 22b. Moreover, both models suffer from torsional cracks, as shown on the far side of the models in Figure 22c,d. Furthermore, unlike the exterior joint, diagonal shear cracks developed on the far side of the interior joint.

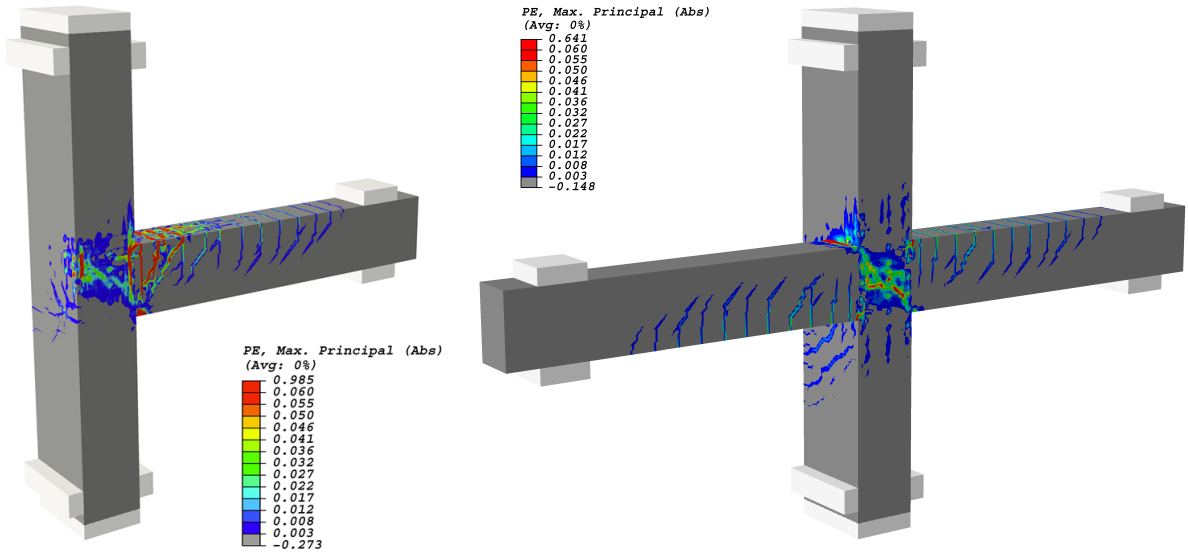

(**a**) (**b**)

Figure 22. *Cont.*

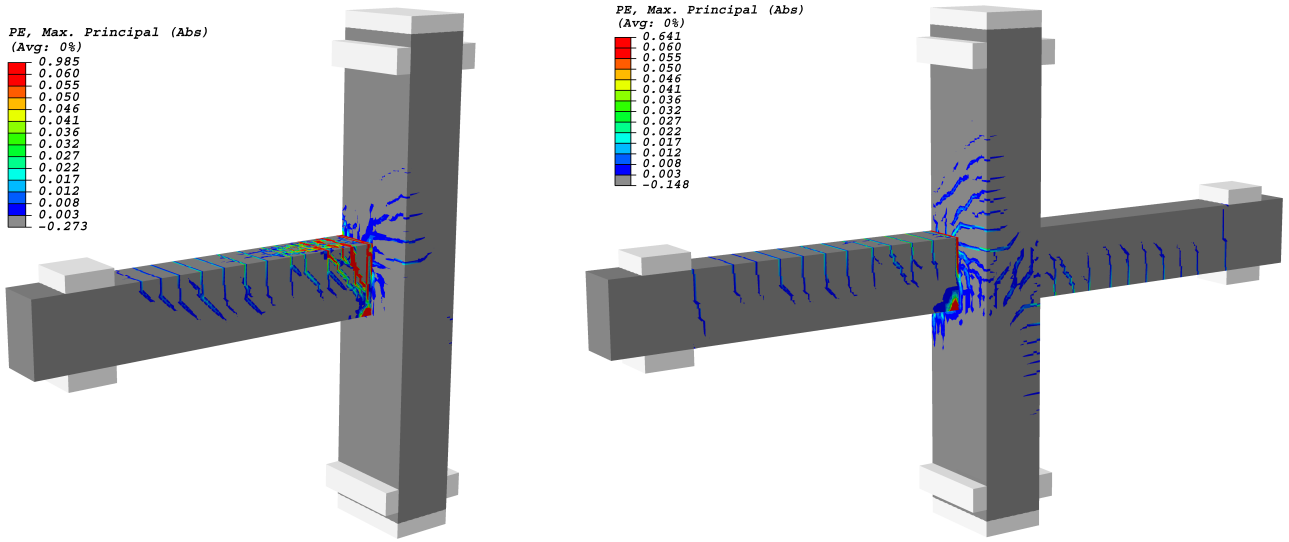

(**c**) (**d**)

Figure 22. Effects of the joint type on the cracking patterns for the eccentric joint models with a joint aspect ratio of 1.125 and a column aspect ratio of 1.5: (**a**) flush side (exterior joint), (**b**) flush side (interior joint), (**c**) far side (exterior joint), and (**d**) far side (interior joint).

Furthermore, by increasing the joint aspect ratio, as shown in Figure 23, the torsional cracks are multiplied and widened. However, the exterior joint model still behaves in a ductile manner where cracks are concentrated at the beam plastic hinge. For the interior joint, on the other hand, it can be seen that the out-of-plane moment became considerable via observing crack depths of the beams in Figure 23b,d, which disappeared in the exterior joint model, as shown in Figure 23a,c. Nevertheless, the increase in the column aspect ratio enhances the cracking behavior, as shown in Figure 24. The shear cracks are eliminated in the joint zone for the exterior joint model, while the beam shear flexural cracks widen, indicating a ductile behavior, as shown in Figure 24a. For the interior joint model, on the other hand, the torsional cracks are reduced, and the joint shear cracks at the far side disappear. In general, the cracking patterns of the models indicate a "strong column–weak beam" response, since the column is still in the elastic stage while the beam or the joint zone have reached their capacity.

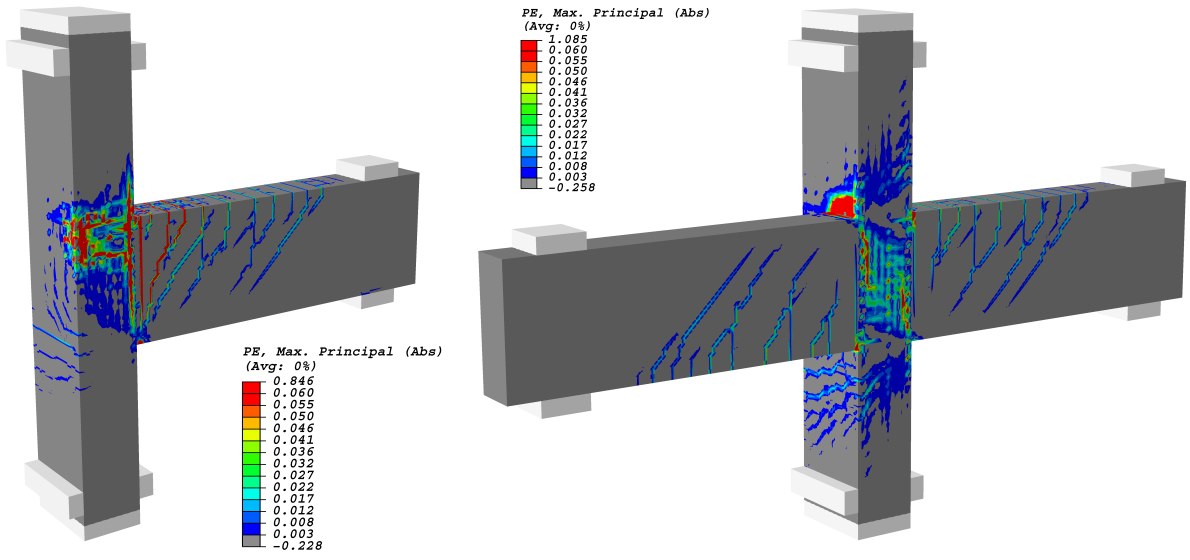

(**a**) (**b**)

Figure 23. *Cont.*

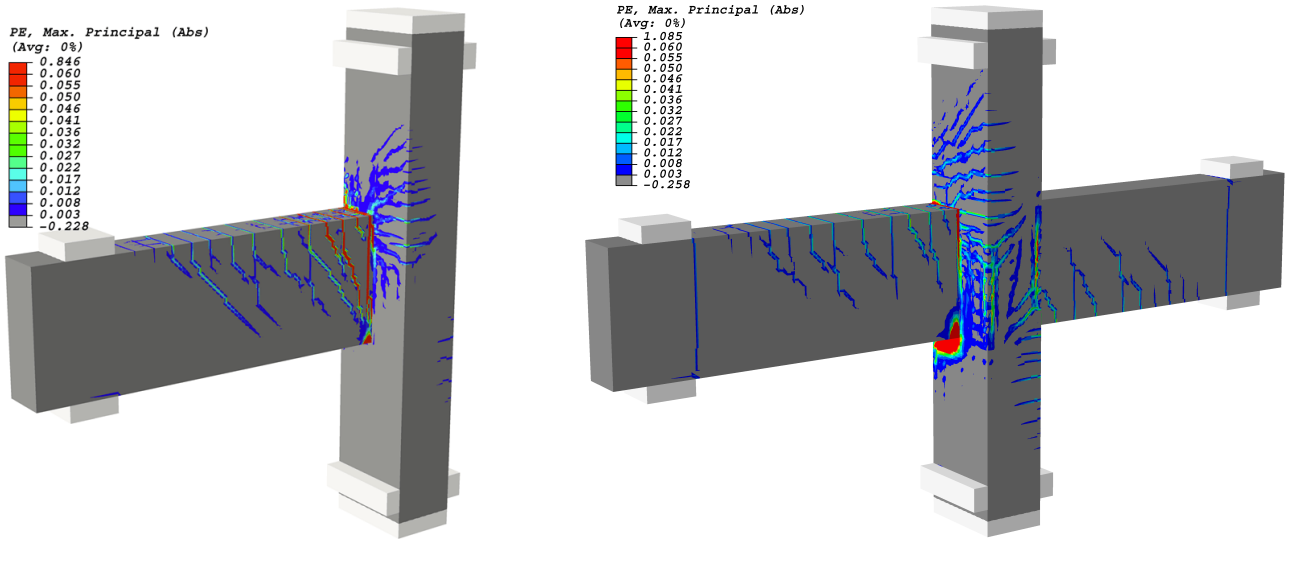

(**c**) (**d**)

Figure 23. Effects of increasing the joint aspect ratio on the cracking patterns for the eccentric joint models with a joint aspect ratio of 2.0 and a column aspect ratio of 1.5: (**a**) flush side (exterior joint), (**b**) flush side (interior joint), (**c**) far side (exterior joint), and (**d**) far side (interior joint).

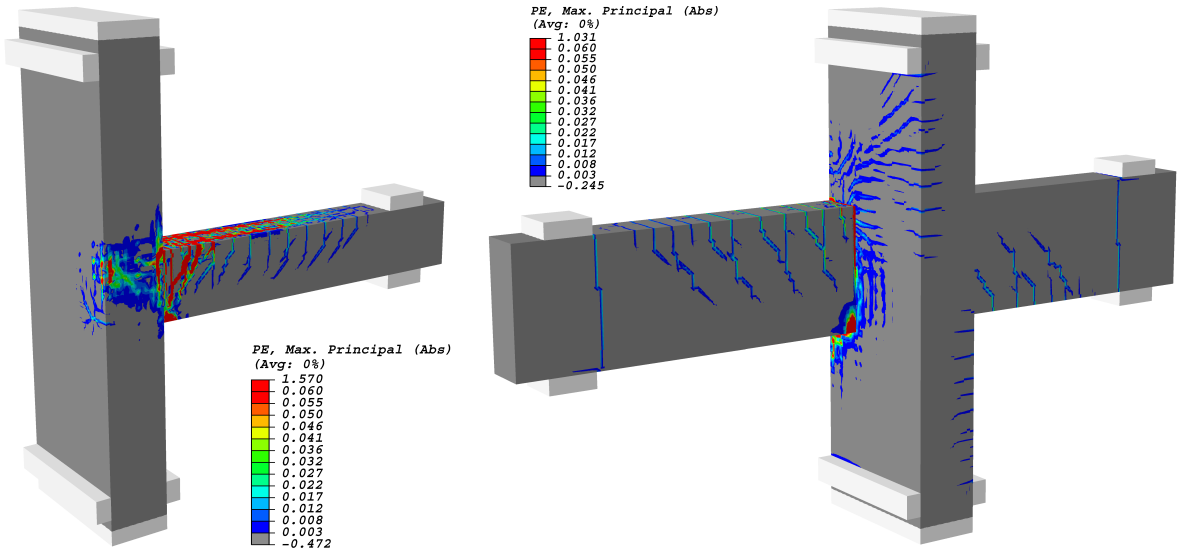

(**a**) (**b**)

Figure 24. Effects of increasing the column aspect ratio on the cracking patterns of the eccentric joint models: (**a**) exterior joint with a joint aspect ratio of 1.125 and a column aspect ratio of 2.5 (flush side), and (**b**) interior joint with a joint aspect ratio of 2.0 and a column aspect ratio of 2.5 (far side).

6. Conclusions

The paper presented here aimed to study the behaviors of the eccentric beam–column subassembly subjected to lateral loading since they have been poorly investigated so far. For this purpose, a finite element analysis has been conducted using the concrete damage plasticity model with an incompatible mesh element type that provides improved accuracy and resolution. FEM results were validated using experimental readings for exterior and interior joints. Afterwards, the calibrated model parameters were utilized to perform a high-resolution parametric study to assess the impact of the geometrical configurations of

the eccentric joints on their behaviors. Based on the observations, the conclusions can be summarized as follows:

1. By combining the concrete damage plasticity with the energy-based uniaxial behavior models, employing the incompatible mesh element type, and considering the column axial load effect on the bond behavior, the global and local behaviors of the exterior and interior eccentric beam–column joints could be predicted precisely, as well as their cracking patterns.
2. In addition to the anticipated flexure, shear, and normal force actions, the eccentric joint is subjected to a torsional moment, which generates additional shear stress on the joint zone, leading to accelerated joint damage. Moreover, the joints experience an out-of-plane deformation, which can potentially compromise the confinement of the beams within the joint, particularly in the case of interior joints.
3. Between the tested parameters, the joint aspect ratio has the dominant impact on the behaviors of the joints by decreasing the joint shear capacity and consequently decreasing the beam–column subassembly capability to develop the beam plastic hinge. Additionally, an increase in the interior joint aspect ratio leads to a higher out-of-plane moment and a loss of joint confinement.
4. An increase in the column aspect ratio resulted in slight enhancements in the joint shear capacity. However, it improves the beam–column subassembly's capability to develop the beam plastic hinge.
5. On average, the shear capacities of the exterior joints are three-fifths of the interior joints. However, ACI-318 and ACI-352 assume four-fifths for this percentage. Furthermore, as the joint aspect ratio exceeds 1.0, they overestimate the exterior joint shear strength.

Author Contributions: Conceptualization, M.A.A.-L. and E.S.; methodology, M.A.A.-L., E.S. and A.A.N.; software, M.A.A.-L.; Analysis, M.A.A.-L., E.S., A.A.N. and W.S.; writing—original draft preparation, M.A.A.-L., E.S. and A.A.N.; writing—review and editing, E.S., A.A.N., M.M.M. and A.G.A.E.-S. All authors have read and agreed to the published version of the manuscript.

Funding: This research did not receive any funding.

Institutional Review Board Statement: Not applicable.

Informed Consent Statement: Not applicable.

Data Availability Statement: The data presented in this study are available on request from the corresponding author.

Acknowledgments: We would like to express our gratitude to Masato NAKAO in the Architecture and Building Science Department at Yokohama National University for providing high-resolution photos of the J−10 specimen in Figure 12. Amr A. Nassr acknowledges Ajman University's financial support.

Conflicts of Interest: The authors declare no conflict of interest.

Sample Availability: Not applicable.

Abbreviations

The following abbreviations are used in this manuscript:

BJ	Beam joint
CDP	Concrete damage plasticity
DR	Drift ratio
FE	Finite element
FEM	Finite element model
J	Joint
RC	Reinforced concrete
STRA	Strain option

Symbols

The following symbols are used in this manuscript:

A_g	Gross area of the column
b_c	Column width
C_d	Material dilatational wave speed
c_{clear}	Clear distance between rebar ribs
D	Bar diameter
d_a	Nominal size of the concrete aggregate
d_b	Beam depth
d_c	Concrete damage in compression, column width
d_{max}	Maximum aggregate size
d_t	Concrete damage in tension
E	Material modulus of elasticity
E_c	Concrete secant modulus of elasticity
E_{ci}	Concert initial modulus of elasticity
E_s	Steel modulus of elasticity
e	Beam Eccentricity
$el\%$	Steel bars elongation
$F_{Translator}$	Bond force per a translator element
f_{cm}	Mean concrete compressive strength
f_{tm}	Main tensile strength
f_t	Tensile strength
f_u	Reinforcement steel's ultimate strength
f_y	Yield stress of steel
G_{fc}	Compressive crushing energy
G_{ft}	Tensile fracture energy
K_c	Tensile-to-compressive meridian ratio
L^e	Smallest element characteristic length
l	Translator elements' spacing
l_{ch}	Mesh size
P_{tr}	Transverse compression force
P_y	Yield load
p	Steel behavior parameter for hardened part
s	Relative slip
s_1, s_2, s_3	Relative slip limits
V_j	Joint shear force
w_t	Crack opening displacement
w_{cr}	Crack opening displacement at the complete release of stress
α_{ts}	Strength level of the interaction stress contribution
Δt	Stability time
δ_{p_y}	Drift ratio at P_y
δ_{p_u}	Drift ratio at load $0.85P_{max}$
ϵ	Plastic potential eccentricity
ε_c	Compressive strain
ε_{cm}	Strain at the compressive strength
ε_c^{pl}	Compressive damaged plastic strain
ε_c^{in}	Compressive inelastic strain
ε_F	Steel fracture strain
ε_t	Tensile strain
ε_{tm}	Strain at the tensile strength
ε_{sh}	Yield hardening onset strain
ε_u	Steel strain at f_u
ε_y	Yield plateau onset strain
γ	Shear stress coefficient
μ	Ductility ratio
ν	Poisson's ratio

$\rho_{s,ef}$	Effective reinforcement ratio
ρ	Material density
σ_t	Tensile stress normal to the crack direction
$\frac{\sigma_{bo}}{\sigma_{co}}$	Biaxial-to-uniaxial compressive strength ratio
τ	Local bond stress
τ_f	Frictional bond stress
τ_{max}	Bond Strength
ψ°	Dilatation angle
$\Omega_{p,tr}$	Bond resistance increase factor for transverse compression force

References

1. Raffaelle, G.S.; Wight, J.K. R/C Eccentric Beam-Column Connections Subjected to Earthquake-Type Loading. Ph.D. Thesis, University of Michigan, Ann Arbor, MI, USA, 1992.
2. Paulay, T.; Park, R.; Preistley, M. Reinforced concrete beam-column joints under seismic actions. *J. Proc.* **1978**, *75*, 585–593.
3. Lafave, J.M.; Shin, M. Performance and design of eccentric reinforced concrete beam-column connections subjected to seismic lateral load reversals. In Proceedings of the Structures Congress Conferance, Austin, TX, USA, 30 April–2 May 2009; pp. 1525–1533. [CrossRef]
4. Kim, J.; LaFave, J.M. Joint Shear Behavior of Reinforced Concrete Beam-Column Connections Subjected to Seismic Lateral Loading. Ph.D. Thesis, Newmark Structural Engineering Laboratory, University of Illinois at Urbana-Champaign, Urbana-Champaign, IL, USA, 2009.
5. Somerville, G.; Taylor, H. The influence of reinforcement detailing on the strength of concrete structures. *Struct. Eng.* **1972**, *50*, 7–19.
6. Kim, J.; LaFave, J.M. A simplified approach to joint shear behavior prediction of RC beam-column connections. *Earthq. Spectra* **2012**, *28*, 1071–1096. [CrossRef]
7. Chun, S.C.; Shin, Y.S. Cyclic testing of exterior beam-column joints with varying joint aspect ratio. *ACI Struct. J.* **2014**, *111*, 693–704. [CrossRef]
8. Joh, O.; Goto, Y.; Shibata, T. Behavior of reinforced concrete beam-column joints with eccentricity. *ACI Spec. Publ.* **1991**, *123*, 317–358.
9. Lawrance, G.; Beattie, G.J.; Jacks, D.H. *The Cyclic Load Performance of an Eccentric Beam-Column Joint*; Technical Report 91-25126; Central Laboratories: Lower Hutt, New Zealand, 1991.
10. Shin, M.S.; LaFave, J.M. Seismic performance of reinforced concrete eccentric beam-column connections with floor slabs. *ACI Struct. J.* **2004**, *101*, 403–412.
11. Kusuhara, F.; Azukawa, K.; Shiohara, H.; Otani, S. Tests of reinforced concrete interior beam-column joint subassemblage with eccentric beams. In Proceedings of the 13th World Conference on Earthquake Engineering, Vancouver, BC, Canada, 1–6 August 2004; Volume 185.
12. LaFave, J.M.; Bonacci, J.F.; Burak, B.; Shin, M. Eccentric beam-column connections. *Concr. Int.* **2005**, *27*, 58–62.
13. RaffaelleE, G.S.; Wight, J.K. Reinforced concrete eccentric beam-column connections subjected to earthquake-type loading. *Struct. J.* **1995**, *92*, 45–55.
14. Matsumoto, T.; Nishihara, H.; Nakao, M.; Castro, J. Experimental study on shear strength of eccentric beam-column joints subjected to seismic loading in super high rise reinforced concrete buildings. In Proceedings of the 15th World Conference on Earthquake Engineering, Lisbon, Portugal, 24–28 September 2012; pp. 6047–6056.
15. Teng, S.; Zhou, H. Eccentric reinforced concrete beam-column joints subjected to cyclic loading. *ACI Struct. J.* **2003**, *100*, 139–148.
16. Lee, H.J.; Ko, J.W. Eccentric reinforced concrete beam-column connections subjected to cyclic loading in principal directions. *ACI Struct. J.* **2007**, *105*, 380–392.
17. Burak, B.; Wight, J.K. Experimental investigation on the seismic behavior of eccentric RC beam-column-slab connections. *ACI Struct. J.* **2008**, *105*, 154–162.
18. Mogili, S.; Kuang, J.S.; Huang, R.Y. Effects of beam-column geometry and eccentricity on seismic behaviour of RC beam-column knee joints. *Bull. Earthq. Eng.* **2019**, *17*, 2671–2686. [CrossRef]
19. Chen, C.C.; Chen, G.K. Cyclic behavior of reinforced concrete eccentric beam-column corner joints connecting spread-ended beams. *ACI Struct. J.* **1999**, *96*, 443–449.
20. Ma, C.; Wang, Z.; Smith, S.T. Seismic performance of large-scale RC eccentric corner beam-column-slab joints strengthened with CFRP systems. *J. Compos. Constr.* **2020**, *24*, 04019066. [CrossRef]
21. Wong, H.F.; Liu, Y.; Luk, S.H.; Lee, P.M.; Kwong, W.H. Effects of eccentricity on seismic behavior of non-seismically designed reinforced concrete beam-column joint. In Proceedings of the 2019 World Congress on Advances in Structural Engineering and Mechanics Conference, Jeju Island, Republic of Korea, 17–21 September 2019; Volume 427.
22. Goto, Y.; Joh, O. Shear resistance of RC interior eccentric beam to column joints. In Proceedings of the 13th World Conference on Earthquake Engineering, Vancouver, BC, Canada, 1–6 August 2004; Volume 649, pp. 1–6.
23. Lee, H.J.; Yu, S.Y. Cyclic response of exterior beam-column joints with different anchorage methods. *ACI Struct. J.* **2009**, *106*, 329–339.

24. Li, B.; Pan, T.C.; Tran, C.T.N. Effects of axial compression load and eccentricity on seismic behavior of non-seismically detailed interior beam-wide column joints. *J. Struct. Eng.-ASCE* **2009**, *135*, 774–784. [CrossRef]
25. Li, B.; Kai, Q.; Xue, W.C. Effects of eccentricity on the seismic rehabilitation performance of non-seismically detailed interior beamwide column joints. *J. Compos. Constr.* **2012**, *16*, 507–519. [CrossRef]
26. ACI. *ASCE Committee 352 Recommendations for Design of Beam-Column Connections in Monolithic Reinforced Concrete Structures (ACI 352R-02) (Reapproved 2010) [s]*; American Concrete Institute: Farmington Hills, MI, USA, 2002; Volume M1.
27. ACI. *Building Code Requirements for Structural Concrete and Commentary (ACI 318-19)*; American Concrete Institute: Farmington Hills, MI, USA, 2019.
28. Rashid, Y. Ultimate strength analysis of prestressed concrete pressure vessels. *Nucl. Eng. Des.* **1968**, *7*, 334–344. [CrossRef]
29. Lubliner, J.; Oliver, J.; Oller, S.; Oñate, E. A plastic-damage model for concrete. *Int. J. Solids Struct.* **1989**, *25*, 299–326. [CrossRef]
30. Lee, J.; Fenves, G.L. Plastic-damage model for cyclic loading of concrete structures. *J. Eng. Mech.* **1998**, *124*, 892–900. [CrossRef]
31. Smith, M. *ABAQUS User's Manual, Version 2018*; Dassault Systemes Simulia Corp: Providence, RI, USA, 2018.
32. Li, Z.X.; Liu, H.; Shi, Y.; Ding, Y. Numerical and analytical investigation on progressive collapse resistance of prestressed precast concrete frame structures. *J. Build. Eng.* **2022**, *52*, 104417. [CrossRef]
33. Pham, A.T.; Tan, K.H.; Yu, J. Numerical investigations on static and dynamic responses of reinforced concrete sub-assemblages under progressive collapse. *Eng. Struct.* **2017**, *149*, 2–20. [CrossRef]
34. Nogales, A.; de la Fuente, A. Numerical-aided flexural-based design of fibre reinforced concrete column-supported flat slabs. *Eng. Struct.* **2021**, *232*, 111745. [CrossRef]
35. Behnam, H.; Kuang, J.; Samali, B. Parametric finite element analysis of RC wide beam-column connections. *Comput. Struct.* **2018**, *205*, 28–44. [CrossRef]
36. Dehghani, A.; Mozafari, A.R.; Aslani, F. Evaluation of the efficacy of using engineered cementitious composites in RC beam-column joints. *Structures* **2020**, *27*, 151–162. [CrossRef]
37. Mirzabagheri, S.; Tasnimi, A.A.; Issa, F. Experimental and numerical study of reinforced concrete interior wide beam-column joints subjected to lateral load. *Can. J. Civ. Eng.* **2018**, *45*, 947–957. [CrossRef]
38. Najafgholipour, M.; Dehghan, S.; Dooshabi, A.; Niroomandi, A. Finite element analysis of reinforced concrete beam-column connections with governing joint shear failure mode. *Lat. Am. J. Solids Struct.* **2017**, *14*, 1200–1225. [CrossRef]
39. Genikomsou, A.S.; Polak, M.A. Finite element analysis of punching shear of concrete slabs using damaged plasticity model in ABAQUS. *Eng. Struct.* **2015**, *98*, 38–48. [CrossRef]
40. Ibrahim, H.A.; Fahmy, M.F.; Wu, Z. Numerical study of steel-to-FRP reinforcement ratio as a design-tool controlling the lateral response of SFRC beam-column joints. *Eng. Struct.* **2018**, *172*, 253–274. [CrossRef]
41. Peng, Z.; Dai, S.B.; Pi, Y.L.; Zhang, Y.C.; Huang, J. Seismic performance of end-plate connections between T-shaped CFST columns and RC beams. *J. Constr. Steel Res.* **2018**, *145*, 167–183. [CrossRef]
42. Xu, L.; Wei, C.; Li, B. Damage evolution of steel-polypropylene hybrid fiber reinforced concrete: Experimental and numerical investigation. *Adv. Mater. Sci. Eng.* **2018**, *2018*, 1719427. [CrossRef]
43. Earij, A.; Alfano, G.; Cashell, K.; Zhou, X. Nonlinear three-dimensional finite-element modelling of reinforced-concrete beams: Computational challenges and experimental validation. *Eng. Fail. Anal.* **2017**, *82*, 92–115. [CrossRef]
44. Faleschini, F.; Bragolusi, P.; Zanini, M.A.; Zampieri, P.; Pellegrino, C. Experimental and numerical investigation on the cyclic behavior of RC beam column joints with EAF slag concrete. *Eng. Struct.* **2017**, *152*, 335–347. [CrossRef]
45. Xiao, K.; Zhang, Q.; Jia, B. Cyclic behavior of prefabricated reinforced concrete frame with infill slit shear walls. *Front. Struct. Civ. Eng.* **2016**, *10*, 63–71. [CrossRef]
46. Yimer, M.A.; Aure, T.W. Numerical investigation of reinforced concrete and steel fiber-reinforced concrete exterior beam-column joints under cyclic loading. *Iran. J. Sci. Technol. Trans. Civ. Eng.* **2022**, *46*, 2249–2273. [CrossRef]
47. Ridwan. Reinforced Concrete Beam-Column Joints Strengthened in Shear with Embedded Bars. Ph.D. Thesis, College of Engineering & Physical Sciences, The University of Birmingham, Birmingham, UK, 2016.
48. Wang, Y.H.; Tang, Q.; Nie, X. Comparative investigation on influences of concrete material constitutive models on structural behavior. *Constr. Build. Mater.* **2017**, *144*, 475–483. [CrossRef]
49. Demirtaş, Y.; Yurdakul, Ö.; Avşar, Ö. Lattice modelling of substandard RC beam-column joints considering localization issues. *Structures* **2023**, *47*, 2515–2530. [CrossRef]
50. Rosso, M.M.; Asso, R.; Aloisio, A.; Di Benedetto, M.; Cucuzza, R.; Greco, R. Corrosion effects on the capacity and ductility of concrete half-joint bridges. *Constr. Build. Mater.* **2022**, *360*, 129555. [CrossRef]
51. *A706/A706M*; ASTM. *Standard Specification for Deformed and Plain Low-Alloy Steel Bars for Concrete Reinforcement*. Technical Report; ASTM International: West Conshohocken, PA, USA, 2016.
52. AIJ. *AIJ Standard for Structural Calculation of Reinforced Concrete Structures*. Architectural Institute of Japan: Tokyo, Japan, 1999.
53. *JIS G 3112*; JIS Steel Bars for Concrete Reinforcement. Japanese Industrial Standards: Tokyo, Japan, 2020.
54. *JIS G 3137*; JIS Steel Bars for Concrete Reinforcement. Japanese Industrial Standards: Tokyo, Japan, 2020.
55. Taerwe, L.; Matthys, S. *Fib Model Code for Concrete Structures 2010*; Ernst & Sohn, Wiley: Berlin, Germany, 2013.
56. Rashid, M.; Mansur, M.; Paramasivam, P. Correlations between mechanical properties of high-strength concrete. *J. Mater. Civ. Eng.* **2002**, *14*, 230–238. [CrossRef]
57. Chen, W.F. *Plasticity in Reinforced Concrete*; J. Ross Publishing: New York, NY, USA, 2007.

58. Vonk, R.A. Softening of Concrete Loaded in Compression. Ph.D. Thesis, Eindhoven University of Technology Eindhoven, Eindhoven, The Netherlands, 1992.
59. German, M.; Pamin, J. FEM simulations of cracking in RC beams due to corrosion progress. *Arch. Civ. Mech. Eng.* **2015**, *15*, 1160–1172. [CrossRef]
60. Wörle, P. Enhanced shear punching capacity by the use of post installed concrete screws. *Eng. Struct.* **2014**, *60*, 41–51. [CrossRef]
61. Bažant, Z.P. Instability, ductility, and size effect in strain-softening concrete. *ASCE J. Eng. Mech. Div.* **1976**, *102*, 331–344. [CrossRef]
62. Krätzig, W.; Pölling, R. An elasto-plastic damage model for reinforced concrete with minimum number of material parameters. *Comput. Struct.* **2004**, *82*, 1201–1215. [CrossRef]
63. Alfarah, B.; López-Almansa, F.; Oller, S. New methodology for calculating damage variables evolution in Plastic Damage Model for RC structures. *Eng. Struct.* **2017**, *132*, 70–86. [CrossRef]
64. Juárez-Luna, G.; Tena-Colunga, A.; Ayala, G. Computational modelling of rc slabs cracking with an embedded discontinuity formulation. *Lat. Am. J. Solids Struct.* **2015**, *12*, 2539–2561.
65. Cornelissen, H. Experiments and theory for the application of fracture mechanics to normal and lightweight concrete. *Fract. Toughness Fract. Energy Concr.* **1986**, 565–575. Available online: https://cir.nii.ac.jp/crid/1570572699262849536 (accessed on 20 June 2023).
66. Hordijk, D.A. Local Approach to Fatigue of Concrete. Ph.D. Thesis, Department of Civil Engineering and Geosciences Delft University Delft, Delft, The Netherlands, 1993.
67. Wosatko, A.; Genikomsou, A.; Pamin, J.; Polak, M.A.; Winnicki, A. Examination of two regularized damage-plasticity models for concrete with regard to crack closing. *Eng. Fract. Mech.* **2018**, *194*, 190–211. [CrossRef]
68. Seok, S.; Haikal, G.; Ramirez, J.A.; Lowes, L.N. High-resolution finite element modeling for bond in high-strength concrete beam. *Eng. Struct.* **2018**, *173*, 918–932. [CrossRef]
69. Lagier, F.; Massicotte, B.; Charron, J.P. 3D nonlinear finite-element modeling of lap splices in UHPFRC. *J. Struct. Eng.-ASCE* **2016**, *142*, 04016087. [CrossRef]
70. Yu, T.; Teng, J.; Wong, Y.; Dong, S. Finite element modeling of confined concrete-II: Plastic-damage model. *Eng. Struct.* **2010**, *32*, 680–691. [CrossRef]
71. Lim, J.C.; Ozbakkaloglu, T.; Gholampour, A.; Bennett, T.; Sadeghi, R. Finite-element modeling of actively confined normal-strength and high-strength concrete under uniaxial, biaxial, and triaxial compression. *J. Struct. Eng.-ASCE* **2016**, *142*, 04016113. [CrossRef]
72. Mander, J.B. Seismic Design of Bridge Piers. Ph.D. Thesis, University of Canterbury, Civil Engineering, Christchurch, New Zealand, 1983.
73. Somma, G.; Vit, M.; Frappa, G.; Pauletta, M.; Pitacco, I.; Russo, G. A new cracking model for concrete ties reinforced with bars having different diameters and bond laws. *Eng. Struct.* **2021**, *235*, 112026. [CrossRef]
74. Huang, Z.; Engström, B.; Magnusson, J. Experimental and analytical studies of the bond behaviour of deformed bars in high strength concrete. In Proceedings of the 4th International Symposium on the Utilization of High Strength/High Performance Concrete, Paris, France, 29–31 May 1996.
75. Li, H.G.; Cen, S.; Cen, Z.Z. Hexahedral volume coordinate method (HVCM) and improvements on 3D Wilson hexahedral element. *Comput. Methods Appl. Mech. Eng.* **2008**, *197*, 4531–4548. [CrossRef]
76. Koutromanos, I. *Fundamentals of Finite Element Analysis: Linear Finite Element Analysis*; John Wiley & Sons: Hoboken, NJ, USA, 2018.
77. Zhou, P.; Cen, S.; Huang, J.; Li, C.; Zhang, Q. An unsymmetric 8-node hexahedral element with high distortion tolerance. *Int. J. Numer. Methods Eng.* **2017**, *109*, 1130–1158. [CrossRef]
78. Kožar, I.; Rukavina, T.; Ibrahimbegović, A. Method of incompatible modes–overview and application. *Građevinar* **2018**, *70*, 19–29.
79. Stern, F.; Wilson, R.V.; Coleman, H.W.; Paterson, E.G. Comprehensive approach to verification and validation of CFD simulations—Part 1: Methodology and procedures. *J. Fluids Eng.* **2001**, *123*, 793–802. [CrossRef]
80. Sun, E.Q. Shear locking and hourglassing in MSC Nastran, ABAQUS, and ANSYS. In Proceedings of the MSC Software Users Meeting, São Paulo, Brazil, July 2006.
81. He, P.; Sun, Q.; Liang, K. Generalized modal element method: Part I Theory and its application to eight-node asymmetric and symmetric solid elements in linear analysis. *Comput. Mech.* **2019**, *63*, 755–781. [CrossRef]
82. He, P.; Sun, Q.; Liang, K. Generalized modal element method: Part II Application to eight-node asymmetric and symmetric solid-shell elements in linear analysis. *Comput. Mech.* **2019**, *63*, 783–804. [CrossRef]
83. Hillerborg, A.; Modéer, M.; Petersson, P.E. Analysis of crack formation and crack growth in concrete by means of fracture mechanics and finite elements. *Cem. Concr. Res.* **1976**, *6*, 773–781. [CrossRef]
84. Bažant, Z.P.; Oh, B.H. Crack band theory for fracture of concrete. *Matériaux Constr.* **1983**, *16*, 155–177. [CrossRef]
85. Bažant, Z.P.; Pijaudier-Cabot, G. Measurement of characteristic length of nonlocal continuum. *J. Eng. Mech.* **1989**, *115*, 755–767. [CrossRef]
86. Volokh, K. Characteristic length of damage localization in concrete. *Mech. Res. Commun.* **2013**, *51*, 29–31. [CrossRef]
87. Carstensen, J.V.; Jomaas, G.; Pankaj, P. Element size and other restrictions in finite-element modeling of reinforced concrete at elevated temperatures. *J. Eng. Mech.* **2013**, *139*, 1325–1333. [CrossRef]

88. Thai, H.T.; Vo, T.P.; Nguyen, T.K.; Pham, C.H. Explicit simulation of bolted endplate composite beam-to-CFST column connections. *Thin-Walled Struct.* **2017**, *119*, 749–759. [CrossRef]
89. Thai, H.T.; Uy, B. Finite element modelling of blind bolted composite joints. *J. Constr. Steel Res.* **2015**, *112*, 339–353. [CrossRef]
90. Paulay, T. Equilibrium criteria for reinforced concrete beam-column joints. *ACI Struct. J.* **1989**, *86*, 635–643.
91. Li, B.; Lam, E.S.S.; Wu, B.; Wang, Y.y. Effect of high axial load on seismic behavior of reinforced concrete beam-column joints with and without strengthening. *ACI Struct. J.* **2015**, *112*, 713–723. [CrossRef]
92. Hwang, S.J.; Lee, H.J.; Liao, T.F.; Wang, K.C.; Tsai, H.H. Role of hoops on shear strength of reinforced concrete beam-column joints. *Struct. J.* **2005**, *102*, 445–453.
93. Chen, G.; Teng, J.; Chen, J.; Xiao, Q. Finite element modeling of debonding failures in FRP-strengthened RC beams: A dynamic approach. *Comput. Struct.* **2015**, *158*, 167–183. [CrossRef]
94. Shin, M.; LaFave, J. Reinforced concrete edge beam-column-slab connections subjected to earthquake loading. *Mag. Concr. Res.* **2004**, *56*, 273–292. [CrossRef]
95. Park, R. Evaluation of ductility of structures and structural assemblages from laboratory testing. *Bull. N. Z. Soc. Earthq. Eng.* **1989**, *22*, 155–166. [CrossRef]
96. Kim, J.; LaFave, J.M. Probabilistic joint shear strength models for design of RC beam-column connections. *ACI Struct. J.* **2008**, *105*, 770–780.
97. Kim, J.; LaFave, J.A. Key influence parameters for the joint shear behaviour of reinforced concrete (RC) beam-column connections. *Eng. Struct.* **2007**, *29*, 2523–2539. [CrossRef]

Disclaimer/Publisher's Note: The statements, opinions and data contained in all publications are solely those of the individual author(s) and contributor(s) and not of MDPI and/or the editor(s). MDPI and/or the editor(s) disclaim responsibility for any injury to people or property resulting from any ideas, methods, instructions or products referred to in the content.